Tectonic evolution of the intra-uplift Vigodi-Gugriana-Khirasra-Netra Fault System in the seismically active Kachchh rift basin, India: Implications for the western continental margin of the Indian plate

Mohamedharoon A. Shaikh [a], Deepak M. Maurya [a,*], Soumyajit Mukherjee [b],
Naimisha P. Vanik [a], Akash Padmalal [a], Laxman S. Chamyal [a]

[a] *Department of Geology, The Maharaja Sayajirao University of Baroda, Vadodara, 390002, Gujarat, India*
[b] *Department of Earth Sciences, Indian Institute of Technology Bombay, Powai, Mumbai, 400076, Maharashtra, India*

ARTICLE INFO

ABSTRACT

The E-W striking Kachchh Rift Basin (KRB) at the western continental margin of Indian plate is located in the northern part of Gujarat state, India. KRB has undergone polyphase deformation owing to changing stress-field since Late Triassic. We establish the kinematic framework along the NW striking intra-uplift Vigodi-Gugriana-Khirasra-Netra Fault System (VGKNFS) located at the western part of the KRB. The VGKNFS consists of 0.25–50 km long, sub-parallel, striated, reactivated dip-slip faults. A total of 1150 fault-slip data consisting of fault planes and striations attitude were recorded from 66 sites (including a single site with systematic joints). Slip-sense of faults was determined by documenting kinematic indicators. Paleostress analysis was carried out using Win-Tensor, T-Tecto, FaultKin and SG2PS to compare and validate the results. The chi-square statistical analysis was undertaken to evaluate how relevant are paleostress analysis results to the present-day compressional stress field. Geophysical investigations were conducted at selected sites using Ground Penetrating Radar (GPR) to understand the shallow subsurface geometry and trace the continuity of faults buried below patchy alluvial cover. 15–17 m long, 2D GPR cross-sections were recorded across faults using monostatic antenna of 200 MHz frequency.

Two major deformation events – D1 and D2 are determined in the present study. The extension event D1 shows W and NW–NNW extension during Late Triassic to Late Cretaceous. It occurred during the rift phase of KRB in response of the break-up of Gondwanaland. The latest event D2 shows NNE–NE compression from Late Cretaceous up to the present. It is interpreted to have developed during post-rift inversion phase, induced by collision of the Indian plate with the Eurasian plate at ~55 Ma.

1. Introduction

Tectonic stresses are mostly responsible for the deformation of the Earth's lithosphere (Zoback et al., 1989). Discrete intra-continental, passive rift systems are marked by extension localized in narrow zones (<100 km wide) e.g., the East African Rift, Baikal rift zone, West Antarctic rift, Rhine graben and Rio Grande rift (Ruppel, 1995). Passive rifting is initiated with lithospheric thinning in response to the far-field extensional stresses that may be generated by plate boundary forces (Ruppel, 1995). Specifically, positive basin inversion tectonics involves reactivation of normal faults, formed during earlier crustal extension, and subsequently as reverse faults during compression (Williams et al., 1989; Schlische, 1995; Sibson, 1995). Examples include the Missour basin in Morocco (Beauchamp et al., 1996), Rio Grande rift of central New Mexico (Ricketts et al., 2015), Kachchh rift basin of western India (Chung and Gao, 1995; Biswas, 2005; Maurya et al., 2016), Sierras Pampeanas of Córdoba in Argentina (Martino et al., 2016) and Faeroe-Shetland basin in northern offshore part of United Kingdom (Davies et al., 2004). Contraction during positive inversion is either oblique or co-axial with the earlier extension direction (Wessex and Weald basins of southern England: Stoneley, 1982; Simpson et al., 1989; Butler and Pullan, 1990; Taranaki basin in New Zealand: King and Thrasher, 1992; Sibson, 1995). Only a few set of pre-existing normal

---

List of abbreviations

ABF	Allah Bund Fault
BO	Borehole Breakouts
DU	Desalpar Uplift
FMS	Focal Mechanism Solution
GF	Gedi Fault
GPR	Ground Penetrating Radar
GUF	Gugriana Fault
IBF	Island Belt Fault
IBU	Island Belt Uplift
KBA	Khirasra Brachy-Anticline
KF	Khirasra Fault
KHF	Katrol Hill Fault
KHRFZ	Katrol Hill Range Fault Zone
KMF	Kachchh Mainland Fault
KMU	Kachchh Mainland Uplift
KRB	Kachchh Rift Basin
NF	Netra Fault
NHRFZ	Northern Hill Range Fault Zone
NKF	North Kathiawar Fault
NKHF	North Khirasra Fault
NPF	Nagar Parkar Fault
RDM	Right Dihedral Method
SWF	South Wagad Fault
VBA	Vigodi Brachy-Anticline
VF	Vigodi Fault
VGKNFS	Vigodi-Gugriana-Khirasra-Netra Fault System
WMBA	Walka Mota Brachy-Anticline
WSM	World Stress Map
WVF	West Vigodi Fault
WU	Wagad Uplift

faults or individual segments of normal fault strands reactivate during inversion demonstrating selective nature of fault reactivation (Sibson, 1995).

Compressive stress regime related to strike-slip and collision/subduction would not exclusively result in reverse faulting and/or inversion in an extensional setting. Reverse faults at the continental rift margins are also produced in response to compressive stress regime associated with the far-field ridge-push forces along seafloor spreading margins. The Fundy rift basin (Canada; Withjack et al., 1995) is an example. Besides, isostatic flexure-induced contraction in uplifted footwall can also result in reverse faulting (e.g., the Rio Grande rift margin: Lewis and Baldridge, 1994).

The seismically active E-W striking Kachchh rift basin (KRB) is located in the state of Gujarat on the western continental margin of India (Biswas and Khattri, 2002; Maurya et al., 2016) (Fig. 1). The Nagar Parkar Fault (NPF) to the north and North Kathiawar Fault (NKF) to the south act as rift shoulders bounding the KRB (Biswas, 2016). The tectonic framework of the KRB is mainly controlled by large, parallel E-W striking intra-basinal faults. Towards the south, these are – Island Belt Fault (IBF), Gedi Fault (GF), South Wagad Fault (SWF), Kachchh Mainland Fault (KMF) (>1200 m throw) and Katrol Hill Fault (KHF) (~732 m maximum throw) (Biswas, 1993; Maurya et al., 2016) (Fig. 1). These major, (sub-)vertical faults show steep flexures and have accommodated large-scale uplifts generated by extension during basin rifting (Late Triassic to Early Jurassic) and are seismically active till today – Island Belt Uplift (IBU), Desalpar Uplift (DU), ~60 km long and ~40 km wide Wagad Uplift (WU), ~193 km long and ~72 km wide Kachchh Mainland Uplift (KMU) (Biswas, 1993) (Fig. 1).

The KMU is sub-divided into four structural zones – the Northern Hill Range Fault Zone (NHRFZ) along the KMF, Katrol Hill Range Fault Zone (KHRFZ) along the KHF, Vigodi-Gugriana-Khirasra-Netra Fault System (VGKNFS) and Bhuj structural low (Biswas, 1993) (Fig. 1). E-W striking, intra-basinal faults are affected and segmented by N, NW, NE, NNW and NNE striking, m to km-scale, transverse faults with dip-/oblique-slip deciphered in the field (Biswas, 1993; Maurya et al., 2003). The NW striking VGKNFS, formed during the basin rift phase, is traceable for ~80 km with a fault zone width of ~10 km. Being located between the E-W striking NHRFZ and KHRFZ at western part of KMU, the VGKNFS has been affected by NW striking, essentially dip-slip faults (Biswas, 1993) (Figs. 1 and 2).

The present structural style of the KRB indicates large-scale, periodic lithospheric deformation owing to varying regional stress field and also, induced local anomalies in the regional stress pattern (Biswas, 2016). KRB, which is the most earthquake prone intra-plate region in India, falls in the highest seismic risk zone–V in seismic hazard zonation map (BIS, 2002; Choudhury et al., 2018) (Fig. 1b). The KRB is characterized by multiple seismic sources as it has witnessed several devastating, moderate-high magnitude intra-plate earthquakes attributed to periodic tectonic movement along the intra-basinal faults. Few examples are: the 1819 Allah Bund earthquake (M_w 7.8; 15 km focal depth; Bilham, 1999; Rajendran and Rajendran, 2001), 1956 Anjar earthquake (M_w 6.1; 15 km focal depth; Chandra, 1977; Chung and Gao, 1995) and 2001 Bhuj earthquake (M_w 7.7; 23 km focal depth; Bendick et al., 2001) (Fig. 1). Therefore, a thorough understanding of behavior of the large-scale, regional stress pattern acting upon the KRB is necessary.

Neotectonic, tectono-geomorphic and paleoseismic aspects of the major E striking intra-basinal faults have been widely discussed in literature. Towards the south, these are – Allah Bund Fault (ABF) (Rajendran and Rajendran, 2001; Padmalal et al., 2019), IBF (Bhattacharya et al., 2019), GF (Maurya et al., 2013), SWF (Kothyari et al., 2016; Maurya et al., 2017), KMF (Chowksey et al., 2011a, b; Shaikh et al., 2019b) and KHF (Patidar et al., 2007, 2008). Probabilistic Seismic Hazard Assessment (PSHA) and Deterministic Seismic Hazard Assessment (DSHA) studies have estimated 1.0–1.1 g of maximum acceleration along the major faults in the KRB (Choudhury et al., 2018).

The aim of the present study is to understand the temporal and spatial evolution of the acting stress field. The existence of two end-member phases of deformation that prevailed since the Mesozoic from extension to compression is discussed. We perform kinematic analysis of brittle structures that provides insights to relate the evolution of faults with the prevalent regional tectonic stress conditions that (re)activated the faults. Inversion of fault-slip data gives the orientation of principal stress axes. Knowledge of the present-day stress field is critical for seismic hazard estimation and mitigation. It is equally important to understand the paleostress field operating at the time of faulting to reconstruct the tectonic evolution of faults in the KRB. The state of tectonic stress can be inferred from the geological and geophysical data e.g., inversion of earthquake Focal Mechanism Solution (FMS), borehole breakouts (BO), drilling-induced fractures, in-situ stress measurements (overcoring and hydraulic fracturing), geological indicators (fault-slip data, volcanic vent alignments) (Zoback, 1992). These provide an accurate estimate of the prevalent paleostress as well as preset-day stress conditions. No attempt has been made so far to reconstruct the paleostress state using geological indicators and to understand the kinematics and brittle tectonics of the KRB. Notably, Vanik et al. (2018) has carried out paleostress analysis using geological indicators along the E striking Katar fault from SW Saurashtra region of Gujarat state, which is ~370 km S of the study area and may not have direct implications.

2. Geological and structural setting of the study area

The greatest uplift in the KRB, the KMU consists of several

Fig. 1. (a) Geological map of the Kachchh Rift Basin (KRB), digitized and redrawn by Patidar (2010). Geological details are after Biswas (1993). The white inward-pointed double arrows represent the orientation of horizontal maximum compressive stress (S_{Hmax}) compiled from the World Stress Map (WSM) project (Heidbach et al., 2016, 2018). The black dotted lines represent structural contours with 1000 feet (values are in negative) contour interval drawn over the top of Precambrian basement (Biswas, 1993). The black dashed lines represent Bouger Gravity Anomaly contours in mGal after Dasgupta et al., 2000. Red stars indicate major earthquakes in the KRB with focal mechanism solutions (Chung and Gao, 1995; Rastogi et al., 2001). IBF: Island Belt Fault, GDF: Gora Dungar Fault, GF: Gedi Fault, SWF: South Wagad Fault, KMF: Kachchh Mainland Fault, VGKNFS: Vigodi-Gugriana-Khirasra-Netra Fault System, KHF: Katrol Hill Fault, NKF: North Kathiawar Fault. IBU: Island Belt Uplift, DU: Desalpar Uplift, WU: Wagad Uplift, KMU: Kachchh Mainland Uplift, NHRFZ: Northern Hill Range Fault Zone, KHRFZ: Katrol Hill Range Fault Zone. Nature of the uplift-bounding faults is based on Biswas (1993); Patidar et al. (2007); Maurya et al. (2013), (2016), (2017). (b) Seismic hazard zonation map of Gujarat state after BIS (2002). (c) Location of Gujarat state with respect to the Indian plate boundaries depicting various tectonic elements (redrawn after Chatterjee et al., 2013). Red, blue and yellow double arrows denote the direction of relative plate motion at convergent, divergent and transform-fault boundaries respectively.

deformation zones as stated earlier. Out of them, the NW striking VGKNFS is one such major brittle shear zone located in the western part of KMU (Biswas, 2016). The tectonically active eastern zone of KMU is separated from its tectonically stable western counterpart by the VGKNFS (Biswas, 1993). We categorize the VGKNFS as an intra-uplift fault system as it is located within the KMU and also to differentiate it

from the uplift-bounding fault systems of the KRB, e.g., the KMF. Around 80 km long VGKNFS exposes the (sub-)parallel strands of step faults – *(i)* NW striking, ~50 km long Vigodi Fault (VF) and its bifurcation; NNW striking, ~7.15 km long West Vigodi Fault (WVF); *(ii)* NW striking, ~45 km long, Gugriana Fault (GUF) with bifurcations; NNW striking, ~10 km long Khirasra Fault (KF); and NW striking, ~8 km long North
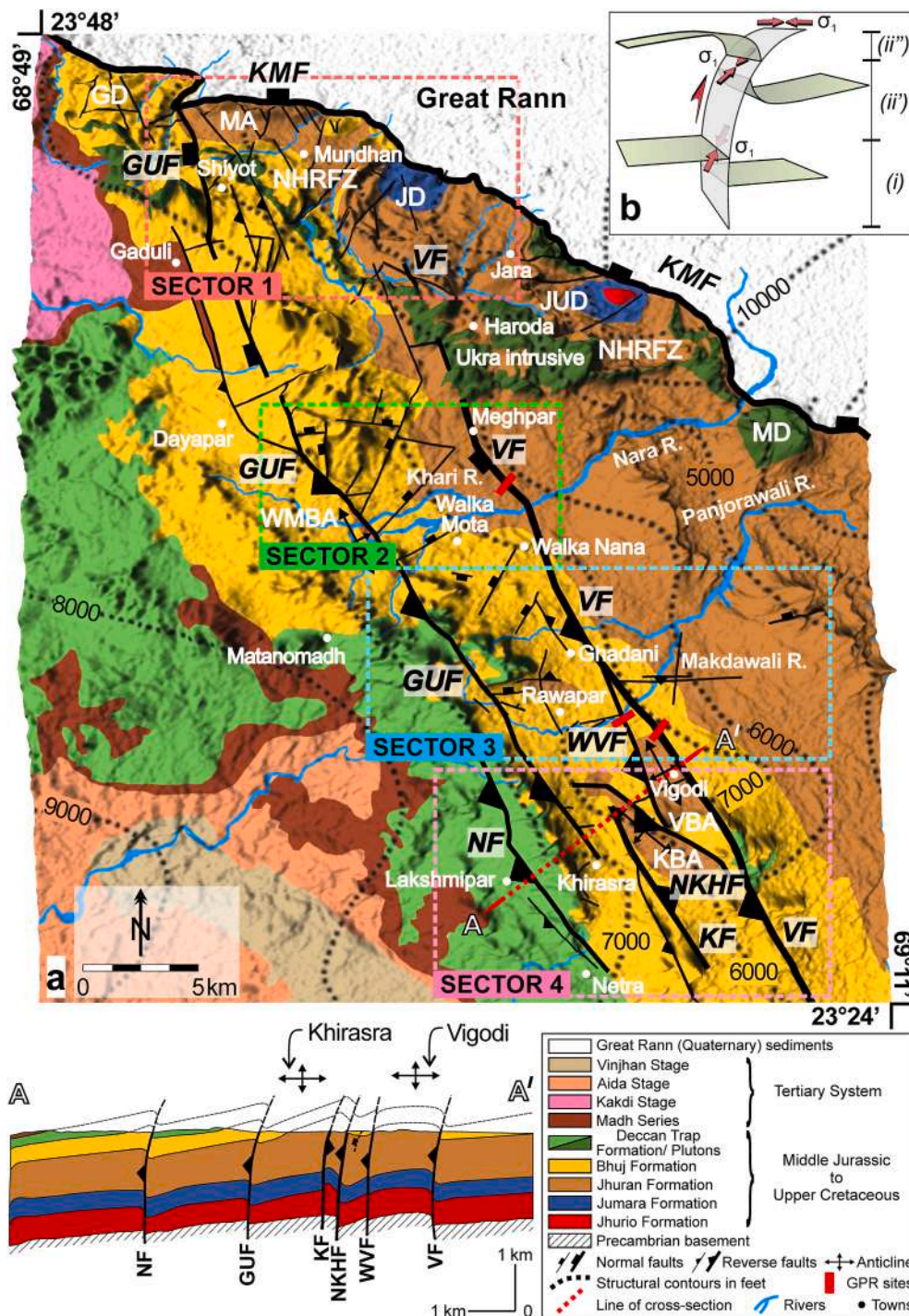
Fig. 2. (a) Tectonic scheme of the VGKNFS as mapped in the present study. The structural contours with 1000 feet (values are in negative) contour interval are drawn over the top of Precambrian basement. The schematic cross-section A–A′ below the map is redrawn from Biswas (1993). VF: Vigodi Fault, WVF: West Vigodi Fault, GUF: Gugriana Fault, KF: Khirasra Fault, NKHF: North Khirasra Fault, NF: Netra Fault, KMF: Kachchh Mainland Fault, NHRFZ: Northern Hill Range Fault Zone, VBA: Vigodi Brachy-Anticline, KBA: Khirasra Brachy-Anticline, WMBA: Walka Mota Brachy-Anticline, GD: Ghuneri dome, MA: Mundhan Anticline, JD: Jara Dome, JUD: Jumara Dome and MD: Manjal Dome. (b) Depth profile of upthrust fault modified and redrawn after fig. 5 of Prucha et al. (1965). The attitude of fault in the segment with convex upward geometry changes from (ii′) high-angle reverse fault at the bottom to (ii″) low-angle reverse fault near the surface. Red, inward-pointed double arrows indicate depth-wise rotation in the orientation of maximum principal stress axis (σ_1). The plunge of σ_1 changes depth-wise with (i) steeper at depth (vertical/near-vertical fault segment), (ii′) moderate plunge in the high-angle reverse fault segment, and (ii″) horizontal/near-horizontal plunge at the surface (low-angle reverse fault segment).

Khirasra Fault (NKHF); and (iii) NNW striking, ~13 km long Netra Fault (NF) (Fig. 2). Besides, there are numerous NW, NE and E striking unnamed cross-faults. NW striking faults are more numerous than the NE striking faults and, NNW and E striking faults are few.

The study area falls in the Survey of India (SOI) topographic sheet numbers 41E/2, 41E/3 and 41A/14 at 1:50,000 scale. Since the study area is vast (~150 km² stretch), we divide the ~80 km long VGKNFS into four sectors. This separation into sectors is necessary to investigate the spatial variation in paleostress field and also to understand the change in kinematic behavior of unnamed cross-faults of varying orientations exposed in the entire study area (Fig. 2). The boundaries of these four sectors are fixed based on the structural continuity of major

NW striking faults in the VGKNFS determined during our extensive field structural investigations (Fig. 2).

The VGKNFS exposes SW dipping major faults showing asymmetric tectonic uplift on their upthrown side, producing a 7–10 km wide, NW striking narrow flexure zone. The VGKNFS is terminated by an E–ESE striking, ~193 km long NHRFZ on its northern extremity and E striking, ~65 km long KHRFZ on its southern extremity. Thus, the VGKNFS makes an acute angle (50–70°) with the uplift-bounding faults (Biswas, 1993). Faults network dies out to the southern margin of Ghuneri dome, Mundhan anticline and Jara dome of the NHRFZ. The length and amount of slip of faults in the VGKNFS are much less than the E striking uplift-bounding faults viz., the KMF. The VGKNFS occurs mainly in

Table 1

Summarized data sheet of GPR survey acquisition and processing parameters for three survey sites. VF: Vigodi Fault, WVF: West Vigodi Fault. See Section 3.2 for discussion.

	Fault	*VF*	*VF*	*WVF*
	Sense of slip	*Reverse dip-slip*	*Normal dip-slip*	*Reverse dip-slip*
	Site	*36*	*Near Site 30*	*34*
	Sector	*3*	*2*	*3*
Acquisition parameters	Nominal antenna frequency (MHz)	200	200	200
	Survey method	Continuous	Continuous	Continuous
	Profile length (m)	17	17	15
	Profile trend	N240°	N30°	N260°
	Samples/scan	512	512	512
	Scans/sec	64	64	64
	Scans/m	80	80	80
	Dielectric constant	7	7	7
	Range (ns)	110	150	150
Processing parameters	Time-zero correction (ns)	–	7	–
	Horizontal background removal (scans)	1023 (between 80 and 512 samples)	1023 (between 00 and 512 samples)	–
	FIR filter (MHz) Low pass boxcar	–	600	400
	High pass boxcar	–	–	50
	Horizontal low pass IIR filter (scans)	3, 5 (between 80 and 512 samples), 7 (between 300 and 512 samples)	5	3
	Linear range gain	1.5	2	–

Mesozoic outcrops affecting the Jhuran and Bhuj Formation consisting dominantly of sandstones and shales with limestones. Faults are also reported to be exposed in the Deccan Trap flows (Biswas, 1993). NE, NNE, N, ENE and E striking secondary faults are often accompanied by dykes in the central and eastern parts of KMU (Biswas, 1993). However, in the western part of KMU, in the study area, VGKNFS is devoid of any dykes except the ~E striking Ukra intrusive to the south of NHRFZ (Biswas, 1993) (Fig. 2). These faults are pre-Tertiary as the VGKNFS neither affects ~E striking Tertiary belt of KMU to south of the Deccan Trap nor in other areas of Tertiary exposures (Biswas, 1993).

NW–NNW striking VF (60–80° dip) is the longest and the easternmost fault of VGKNFS (Fig. 2). The throw of VF is estimated to be 45–61 m (Biswas, 1993). The discontinuous NW–NNW striking GUF originates in the saddle region between the Ghuneri dome and Mundhan anticline (Fig. 2). The GUF dips 60–85° towards SW with the maximum throw is around the locality Gugriana. NW–NNW striking KF and NKHF are the branches of GUF extending to the SE (Biswas, 1993) (Fig. 2). The NNW–NW striking NF dips 70–75° towards the upthrown SW side. The NF is of post-Paleocene in age (Biswas, 1993). NW striking VGKNFS is also riddled with a network of NE, NW and E striking small-scale, unnamed cross-faults (Fig. 2). They run for tens of meters to few kms and then die out/truncate in the deformation zone of NW striking major faults. Follow Section 1 (Supplementary data) for more details on the geological background of the VGKNFS.

Basement-controlled tectonics has shaped out the present geometry of VGKNFS (Prucha et al., 1965; Biswas, 1993). All the four major fault strands are the basement faults. They act as plunging upthrust due to their differential vertical uplift along the entire length of the individual fault strands (Fig. 2b). The fault geometry is deduced based on the present structural studies and geological work carried out by Biswas (1993). The geometry and attitude of upthrust faults change depth-wise in the sense that they are *(i)* initially vertical/near-vertical at depth, but becomes *(ii)* convex upward with reverse slip (anti-listric) as they grow upward, and eventually rotate toward the downthrown block (Miller and Mitra, 2011). The upthrust faults also show drape-folding of sedimentary units over the displaced basement rocks.

3. Methods

To understand the kinematic evolution of VGKNFS, detailed structural analysis at regional scale was carried out. We performed *(i)*

paleostress analysis using collected fault-slip data (Sections 3.1, 4), *(ii)* statistical analysis using derived compressional stress directions of major and unnamed cross-faults (Section 6.4), and *(iii)* shallow subsurface geophysical investigations using Ground Penetrating Radar (GPR) (Sections 3.2, 5).

3.1. Paleostress analysis

Paleostress analysis is now a well-practiced technique that has widespread consideration in order to understand different tectonic events (Federico et al., 2014; Giambiagi et al., 2017; Vanik et al., 2018). The results are represented in the form of a paleostress tensor made up of three mutually perpendicular principal stress axes, viz. the maximum principal stress axis (σ_1), intermediate principal stress axis (σ_2) and minimum principal stress axis (σ_3); and the stress ratio (R). The parameter $R = (\sigma_2 – \sigma_3)(\sigma_1 – \sigma_3)^{-1}$ defines the shape of stress ellipsoid (Angelier, 1994; Delvaux et al., 1997). Furthermore, we indicate the orientation of the maximum and minimum horizontal principal stress (S_{Hmax} and S_{hmin}).

Spatially or temporally varying stress regime may work on the same fault plane. Temporally, the fault may reactivate multiple times preserving several mutually superimposed striations orientations. Alternatively, the fault may show spatial variation in the stress orientations. Such fault-slip data are called heterogeneous (Yamaji and Sato, 2019). Multiple stress states are required to explain the heterogeneous fault-slip data. Fault-slip data are called homogeneous if a single stress state explains the whole fault-slip dataset (Yamaji and Sato, 2019).

We measured the fault-slip data comprising of attitude of fault planes and slickenside lineations. The slip-sense of faults was determined by observing various slickenside kinematic indicators. To accurately compute the paleostress state belonging to distinct tectonic events, to minimize the uncertainties and to cross-examine and increase the reliability of results, we used several open-source computer programmes that work with different procedures, viz., Win_Tensor (v.5.8.8) (Delvaux and Sperner, 2003), T-Tecto studio X5 (Zalohar and Vrabec, 2007), FaultKin (v.8.0) (Marrett and Allmendinger, 1990; Allmendinger et al., 2012) and SG2PS (Sasvári and Baharev, 2014). Several attempts have been made to analyze and compare the results of paleostress analysis performed using multiple algorithms on natural datasets (Sippel et al., 2009; Federico et al., 2014; Vanik et al., 2018; Maestro et al., 2018). Using the aforementioned four programmes, we incorporated three

Table 2

Table summarizing paleostress analysis results for the studied sites at the VGKNFS. See Section 4 for discussion.

Software: Method:					Win_Tensor[o] RDM[s]			T-Tecto[p] RDM				FaultKin[q] Linked Bingham statistics			SG2PS[r] Methodology of Angelier (1990)			S_{Hmax}[x]/ S_{hmin}[y]	R[/z]	Stress regime
Site no.	Fault	SOS[j]	Lithology	nt[n]	σ_1[t]	σ_2[u]	σ_3[v]	σ_1	σ_2	σ_3	D[w]	σ_1	σ_2	σ_3	σ_1	σ_2	σ_3			
SECTOR 1 (Total number of sites investigated: 14, Sites included in fault-slip analysis: 08, Sites exposing non-striated faults: 06)																				
33	GUF[a]	N[j]	Bhuj sst[l]	19	006∠72	154∠16	247∠09	003∠76	225∠11	133∠09	0.1	013∠71	155∠15	248∠11	214∠67	315∠04	047∠22	*071*	0.52	PE*
14	UF[b]	R[k]	Bhuj sst	15	265∠27	000∠10	108∠61	290∠33	021∠02	113∠56	0.2	280∠26	185∠10	076∠62	206∠13	302∠24	091∠62	074	2.19	TP$
15	UF	R	Bhuj sst	43	303∠23	212∠02	118∠67	281∠13	012∠02	110∠77	0.8	298∠30	031∠06	131∠60	320∠18	227∠09	112∠69	124	2.53	PC∞
16	VF[c]	R	Jhuran sst[m]	20	226∠26	326∠19	088∠56	261∠44	154∠17	048∠41	0.2	256∠30	157∠15	044∠56	199∠08	292∠21	090∠67	024	2.03	TP
74	UF	N	Jhuran sst	09	102∠71	208∠05	300∠18	270∠86	098∠04	008∠01	0.1	107∠70	212∠05	304∠19	090∠74	198∠05	289∠15	*126*	0.62	PE
71	UF	N	Bhuj sst	09	316∠60	212∠08	118∠29	307∠44	209∠08	111∠44	0.7	317∠61	212∠08	117∠28	314∠69	180∠15	086∠14	*108*	0.85	TT@
73	UF	N	Jhuran sst	06	113∠65	022∠01	292∠25	151∠75	026∠09	294∠12	0.1	129∠65	024∠07	291∠24	113∠74	001∠06	269∠15	*105*	0.74	PE
91	UF	N	Bhuj sst	08	129∠62	028∠06	295∠27	151∠75	026∠09	294∠12	0.1	320∠24	035∠07	141∠65	138∠73	019∠09	286∠15	*115*	0.66	PE
SECTOR 2 (Total number of sites investigated: 28, Sites included in fault-slip analysis: 21, Sites exposing non-striated faults: 07)																				
44	VF	N	Jhuran sst	08	055∠73	172∠08	264∠15	270∠86	062∠03	152∠02	0.1	061∠70	163∠04	255∠20	070∠75	176∠04	267∠15	*079*	0.52	PE
18	VF	N	Jhuran sst	81	066∠58	165∠06	259∠32	076∠76	179∠03	270∠14	0.2	070∠61	171∠06	264∠28	081∠72	188∠06	280∠17	*091*	0.68	PE
17	VF	N	Jhuran sst	50	075∠68	169∠02	260∠22	076∠76	179∠03	270∠14	0.2	64∠71	165∠05	261∠19	085∠73	191∠05	283∠16	*083*	0.48	PE
22	VF	N	Jhuran sst	13	267∠67	176∠00	086∠23	272∠86	005∠00	095∠04	0.2	259∠71	356∠02	087∠18	260∠65	083∠24	352∠01	*082*	0.58	PE
23	VF	N	Jhuran sst	14	251∠57	343∠01	073∠33	276∠55	185∠01	094∠35	0.5	253∠56	162∠01	071∠34	246∠69	145∠04	053∠21	*067*	1.11	TT
45	VF	N	Jhuran sst	06	251∠55	343∠02	075∠35	300∠76	198∠03	108∠14	0.1	250∠55	343∠02	075∠35	260∠70	359∠03	090∠20	*081*	1.10	TT
30	VF	N	Jhuran sst	13	270∠60	162∠10	067∠28	277∠55	185∠01	094∠35	0.7	268∠60	165∠07	071∠29	265∠68	110∠21	017∠09	*063*	0.88	TT
24	VF	R	Jhuran sst	21	247∠16	343∠17	117∠66	113∠02	204∠12	014∠78	0.9	277∠19	182∠16	054∠65	228∠08	321∠15	112∠73	061	2.33	PC
20	GUF	R	Bhuj sst	15	272∠17	181∠04	079∠73	248∠02	157∠12	347∠78	0.8	267∠11	176∠05	062∠78	307∠20	215∠04	115∠70	094	2.46	PC
19	GUF	R	Bhuj sst	41	244∠10	337∠20	127∠67	101∠02	191∠02	326∠87	0.9	261∠16	170∠06	060∠73	242∠12	334∠07	093∠76	060	2.46	PC
21	GUF	R	Bhuj sst	11	257∠37	166∠01	074∠52	261∠65	003∠05	095∠24	0.1	259∠40	352∠03	086∠50	257∠62	160∠03	068∠27	081	1.69	PS#
04	GUF	R	Bhuj sst	29	230∠10	139∠04	025∠79	113∠02	023∠02	247∠87	0.9	235∠11	144∠06	025∠78	214∠11	305∠03	050∠79	051	2.52	PC
05	GUF	R	Bhuj sst	26	230∠23	139∠01	047∠67	239∠13	149∠02	050∠77	0.7	240∠19	149∠03	050∠70	202∠16	294∠10	055∠71	051	2.46	PC
06	GUF	R	Bhuj sst	17	251∠29	160∠01	068∠61	295∠13	026∠02	124∠77	0.9	250∠26	341∠04	079∠63	209∠18	302∠09	057∠69	072	2.24	TP
58	GUF	R	Bhuj sst	07	274∠09	183∠03	077∠80	321∠02	231∠02	098∠87	0.9	258∠10	167∠02	064∠79	250∠09	340∠02	079∠81	176	2.48	PC
07	GUF	R	Bhuj sst	24	226∠12	136∠02	036∠78	228∠23	319∠2	053∠67	0.7	233∠16	142∠04	038∠73	219∠13	310∠04	058∠76	047	2.50	PC
08	GUF	R	Bhuj sst	42	227∠26	319∠05	059∠64	166∠00	256∠12	075∠78	1.0	236∠32	142∠06	043∠58	187∠14	281∠17	059∠67	043	2.23	TP
76	UF	N	Bhuj sst	06	163∠68	258∠02	349∠22	219∠65	118∠05	026∠25	0.2	187∠66	088∠04	357∠23	175∠72	053∠10	321∠15	166	0.49	PE
75	UF	N	Bhuj sst	06	113∠71	203∠00	293∠19	152∠76	325∠14	055∠02	0.0	129∠68	022∠07	289∠20	133∠73	002∠11	270∠13	*104*	0.64	PE
09	UF	N	Bhuj sst	12	114∠60	242∠20	341∠22	120∠44	227∠17	333∠41	0.9	126∠64	239∠11	334∠23	139∠73	250∠06	342∠15	*160*	0.67	PE
100	J[g]	–	Jhuran sst	21	091∠81	200∠03	290∠09	003∠76	184∠14	094∠00	0.1	–	–	–	–	–	–	*281*	0.99	TT
SECTOR 3 (Total number of sites investigated: 43, Sites included in fault-slip analysis: 29, Sites exposing non-striated faults: 14)																				
01	GUF	R	Bhuj sst	22	248∠26	151∠15	034∠59	248∠02	157∠12	347∠78	0.8	235∠25	142∠06	038∠64	304∠13	211∠13	078∠71	080	2.59	PC
02	GUF	R	Bhuj sst	18	223∠18	313∠00	044∠72	114∠17	023∠05	277∠73	1.0	250∠16	157∠10	037∠71	216∠12	309∠13	084∠72	043	2.50	PC
53	GUF	R	Bhuj sst	05	227∠20	320∠08	070∠68	253∠13	344∠02	082∠77	0.7	236∠22	145∠04	046∠68	200∠16	292∠07	044∠72	043	2.33	PC
67	GUF	R	Bhuj sst	15	036∠05	126∠03	242∠84	293∠23	024∠02	118∠67	0.5	030∠04	121∠05	265∠83	038∠09	308∠02	203∠81	036	2.51	PC
27	VF	R	Bhuj sst	21	210∠24	306∠12	061∠63	251∠34	129∠38	008∠34	0.2	248∠24	144∠29	011∠51	173∠02	264∠27	078∠63	020	2.31	PC

(continued on next page)

Table 2 (*continued*)

Software:					Win_Tensor[o]			T-Tecto[p]				FaultKin[q]			SG2PS[r]			S_Hmax[x]/	R'[z]	Stress
Method:					RDM[s]			RDM				Linked Bingham statistics			Methodology of Angelier (1990)			S_hmin[y]		regime
Site no.	Fault	SOS[i]	Lithology	nt[n]	σ_1[t]	σ_2[u]	σ_3[v]	σ_1	σ_2	σ_3	D[w]	σ_1	σ_2	σ_3	σ_1	σ_2	σ_3			
28	VF	R	Bhuj sst	12	215∠07	123∠17	326∠72	281∠13	012∠02	110∠77	1.0	191∠07	283∠15	075∠74	213∠09	121∠13	335∠74	038	2.52	PC
87	VF	R	Bhuj sst	06	210∠29	304∠06	045∠60	150∠02	240∠02	015∠87	0.9	223∠32	130∠04	033∠58	222∠19	314∠05	058∠70	024	1.93	TP
36	VF	R	Bhuj sst	30	240∠27	149∠00	059∠63	251∠33	348∠10	092∠55	0.3	242∠26	333∠02	067∠64	180∠13	274∠17	055∠69	061	2.27	PC
37	VF	R	Bhuj sst	15	248∠10	156∠13	016∠74	275∠13	185∠01	092∠77	1.0	241∠07	332∠05	101∠81	239∠09	148∠08	018∠78	070	2.50	PC
35	WVF[d]	R	Bhuj sst	17	226∠20	129∠18	000∠63	180∠23	085∠11	331∠65	0.9	266∠15	169∠24	025∠61	015∠00	285∠22	105∠68	046	2.31	PC
34	WVF	R	Bhuj sst	43	234∠22	327∠08	077∠66	267∠13	174∠12	043∠73	0.8	256∠22	161∠12	045∠65	208∠12	301∠14	080∠72	048	2.36	PC
77	SDB[h]	N	Bhuj sst	06	233∠56	058∠34	326∠02	226∠76	339∠06	071∠13	0.9	231∠51	050∠39	140∠00	242∠75	064∠15	334∠00	140	0.79	TT
62	UF	N	Bhuj sst	06	333∠70	072∠03	163∠20	302∠76	054∠5	145∠13	0.1	325∠66	068∠06	161∠23	317∠74	069∠06	160∠15	165	0.72	PE
12	UF	R	Bhuj sst	18	041∠16	134∠10	255∠71	016∠13	286∠02	188∠77	0.9	038∠15	130∠06	240∠74	046∠14	137∠05	247∠75	037	2.44	PC
03	UF	R	Bhuj sst	33	057∠13	147∠01	241∠77	113∠02	204∠12	014∠78	0.8	052∠08	143∠07	273∠79	037∠13	128∠04	234∠77	057	2.49	PC
48	UF	N	Bhuj sst	07	179∠64	086∠01	356∠26	143∠44	052∠01	320∠46	0.7	176∠64	266∠00	356∠26	163∠69	053∠07	320∠19	177	0.50	PE
32	UF	N	Bhuj sst	08	157∠54	260∠09	357∠33	124∠54	224∠07	319∠35	0.3	159∠53	263∠11	000∠35	121∠29	217∠11	325∠29	016	1.19	TT
10	UF	R	Bhuj sst	16	192∠14	101∠01	007∠76	260∠02	170∠02	035∠87	0.9	196∠17	105∠04	003∠73	181∠13	272∠03	013∠77	012	2.48	PC
31	UF	R	Bhuj sst	12	067∠16	159∠07	270∠73	039∠02	309∠12	139∠78	0.9	067∠16	158∠05	264∠73	119∠19	028∠02	291∠71	065	2.35	PC
51	UF	N	Bhuj sst	06	144∠69	021∠12	287∠17	270∠86	134∠03	044∠03	0.1	134∠69	025∠07	292∠19	123∠73	002∠09	269∠15	109	0.49	PE
50	UF	N	Bhuj sst	08	121∠69	029∠01	298∠21	000∠86	188∠04	098∠01	0.2	135∠67	031∠06	298∠22	076∠73	186∠06	278∠16	114	0.53	PE
49	UF	N	Bhuj sst	11	126∠64	026∠05	294∠25	124∠54	024∠07	290∠35	0.6	129∠63	026∠06	293∠26	128∠73	018∠06	286∠16	107	0.67	PE
25	UF	N	Bhuj sst	15	124∠72	027∠02	296∠18	000∠86	152∠03	242∠02	0.1	124∠71	027∠02	296∠19	113∠74	355∠08	263∠14	116	0.63	PE
26	UF	N	Bhuj sst	16	136∠72	028∠06	296∠17	131∠65	031∠05	299∠25	0.4	134∠72	026∠06	294∠17	124∠75	010∠06	278∠14	112	0.57	PE
11	UF	N	Bhuj sst	36	111∠65	211∠05	303∠25	078∠75	202∠08	294∠12	0.2	099∠66	206∠08	300∠23	112∠70	240∠13	334∠15	125	0.61	PE
29	UF	N	Bhuj sst	09	100∠68	208∠07	300∠21	077∠76	179∠03	270∠14	0.1	102∠66	204∠05	297∠23	101∠72	205∠04	296∠17	120	0.61	PE
61	UF	N	Bhuj sst	13	066∠75	198∠10	290∠11	078∠75	214∠11	306∠10	0.2	075∠74	205∠11	298∠12	066∠75	203∠11	295∠10	119	0.54	PE
60	UF	N	Bhuj sst	07	346∠73	117∠11	210∠13	002∠65	094∠01	184∠25	0.3	357∠77	115∠06	206∠12	006∠74	112∠04	203∠16	027	0.53	PE
38	UF	R	Bhuj sst	12	171∠18	080∠04	338∠72	113∠02	023∠02	247∠87	0.9	176∠15	086∠03	345∠75	150∠15	241∠05	349∠74	174	2.45	PC
SECTOR 4 (Total number of sites investigated: 15, Sites included in fault-slip analysis: 08, Sites exposing non-striated faults: 07)																				
39	GUF	R	Bhuj sst	32	256∠22	347∠02	081∠68	267∠13	358∠02	096∠77	0.7	264∠25	354∠01	087∠64	064∠22	330∠10	217∠66	073	2.45	PC
41	GUF	R	Bhuj sst	16	243∠24	152∠02	057∠66	032∠02	302∠02	170∠87	1.0	238∠25	329∠02	063∠64	248∠18	157∠03	057∠72	065	2.20	TP
40	GUF	R	Bhuj sst	14	246∠21	154∠05	052∠68	032∠02	122∠02	260∠87	1.0	246∠26	155∠02	060∠64	240∠18	331∠02	067∠72	074	2.45	PC
56	UF	N	Bhuj sst	10	026∠62	129∠07	223∠27	276∠86	063∠03	153∠22	0.0	025∠58	123∠05	216∠31	020∠70	116∠02	207∠20	041	0.90	TT
57	KF[e]	R	Bhuj sst	06	072∠20	342∠01	248∠70	199∠12	108∠01	010∠77	1.0	055∠21	149∠10	263∠66	085∠14	353∠10	227∠73	074	2.43	PC
42	KF	R	Bhuj sst	24	069∠22	335∠08	226∠66	008∠01	098∠12	275∠78	1.0	059∠17	151∠08	264∠71	075∠15	343∠07	228∠73	076	2.51	PC
68	NF[f]	R	Bhuj sst	07	246∠33	338∠03	073∠57	227∠13	317∠02	056∠77	1.0	248∠30	157∠03	62∠59	245∠18	336∠03	075∠71	061	2.09	TP
89	NF	R	Bhuj sst	06	252∠27	162∠00	072∠63	272∠02	002∠02	138∠87	0.9	255∠25	164∠02	069∠64	253∠18	344∠03	083∠72	072	2.35	PC

Note. *Pure Extensive (Delvaux et al., 1997). $Transpressive (Delvaux et al., 1997). ∞Pure Compressive (Delvaux et al., 1997). @Transtensive (Delvaux et al., 1997). #Pure Strike-Slip (Delvaux et al., 1997).

[a] Gugriana Fault.
[b] Unnamed Fault.
[c] Vigodi Fault.
[d] West Vigodi Fault.
[e] Khirasra Fault.
[f] Netra Fault.
[g] Joints.
[h] Slipped Deformation Band.
[i] Sense of Slip (inferred from field observations).
[j] Normal dip-slip.
[k] Reverse dip-slip.
[l] Bhuj sandstone.
[m] Jhuran sandstone.
[n] Number of collected fault-slip data.
[o] Win_Tensor (v.5.8.8) (Delvaux and Sperner, 2003).

[p] T-Tecto studio X5 (Zalohar and Vrabec, 2007).

[q] FaultKin (v.8.0) (Marrett and Allmendinger, 1990; Allmendinger et al., 2012).

[r] SG2PS (Sasvári and Baharev, 2014).

[s] Right Dihedral Method.

[t] Trend and plunge of maximum (σ_1) principal stress axes (in degrees with respect to north geographical direction).

[u] Trend and plunge of intermediate (σ_2) principal stress axes (in degrees with respect to north geographical direction).

[v] Trend and plunge of minimum (σ_3) principal stress axes (in degrees with respect to north geographical direction) ($\sigma_1 \geq \sigma_2 \geq \sigma_3$).

[w] Parameter D of T-Tecto: similar to stress ratio (R) defined by Delvaux et al. (1997).

[x] Orientation of maximum horizontal principal stress (in degrees with respect to north geographical direction, obtained from Win_Tensor software) in respective areas of reverse faulting stress regime.

[y] Orientation of minimum horizontal principal stress (in degrees with respect to north geographical direction, obtained from Win_Tensor software) in respective areas of normal faulting stress regime.

[z] Stress regime index (Delvaux et al., 1997).

types of brittle structures in the procedure: *(i)* fault planes with slick-enside lineations, *(ii)* deformation bands with striated, principal slip surface, and *(iii)* systematic joints. In the fault damage zone, it is assumed that the tilting of beds is presumably synchronous to faulting. We observed negligible tilt of beds in the narrow deformation zone, therefore, there was no need to un-tilt the bedding from the resultant paleostress tensors.

3.1.1. Fundamental assumptions

Paleostress analysis presumes several points (Etchecopar et al., 1981; Simón, 2019). *(i)* As per the Wallace-Bott hypothesis, fault plane slips in the direction of maximum resolved shear stress (τ_{max}) (Wallace, 1951; Bott, 1959). This assumption holds true in our studies as it is exemplified by a rather small percentage of fault-slip data showed the misfit angle $\geq 20°$. *(ii)* Slip failure occurs in homogeneous and isotropic rock bodies. *(iii)* Stress field is spatially and temporally homogeneous (Kaven et al., 2011). In order to accomplish this assumption, fault-slip measurements were collected from each of the sites and data were not mixed from different sites. Only long, straight, parallel oriented striations indicative of stress homogeneity were measured and included in the dataset. *(iv)* Slip occurs on faults of varied orientations and thus, faults are not necessarily oriented in the optimum direction with respect to the principal stresses as predicted from Coulomb failure criterion (Twiss and Unruh, 1998). *(v)* The rock volume experiencing faulting is large compared to the scale of faults and displacement along the faults is small compared to fault dimensions (Simón, 2019). In order to fulfil this assumption, sufficient number of fault-slip data were collected from each of the sites.

3.1.2. Win_Tensor

We applied Right Dihedron Method (RDM) implemented in Win_Tensor (v.5.8.8) (Delvaux and Sperner, 2003). RDM is a graphical method to determine the principal stress axes orientations in fault-slip analysis. The derived stress tensor resembles the beach-ball diagram generated by earthquake focal mechanisms. Fault-slip data are plotted on equal area projection. The orientation of compressional (P-quadrant) and extensional (T-quadrant) quadrants are defined for each of the fault-slip data according to the fault plane and striations attitudes. The orientation of σ_1 lies in the P-quadrant, while the orientation of σ_3 is constrained to the T-quadrant. An assumption in this technique that applies to the homogeneous fault-slip dataset is that the faults active in the same stress field have a common intersection of P- and T-quadrants. The stereonet is divided into four dihedra, which are created by the fault plane and intersecting auxiliary plane orthogonal to fault plane. The striation is the pole to auxiliary plane. Of the four dihedra, a pair of two opposed quadrants are compressional and the other pair of opposed quadrants are extensional. This process is repeated for all the fault-slip data. Finally, all the dihedra generated from the whole fault-slip dataset are superimposed. This iteration process progressively narrows down the areas of compression and extension. The common, small area of stereonet for which all the quadrants of compression or extension intersect/superpose are the orientations of σ_1 and σ_3 axes, respectively.

The term "stress regime", which varies as a function of R has been defined by Delvaux et al. (1997) to express the type of stress tensor. Plunge of principal stress axes defines the three end-members of stress regime, viz., σ_1 vertical: extensional regime, σ_3 vertical: compressional regime, and σ_2 vertical: strike-slip regime (Delvaux et al., 1997; Giambiagi et al., 2016). In between these three end-members, the stress regime also varies as a function of R. These subsidiary types of stress regime are expressed numerically using stress index (R$'$) by Delvaux et al. (1997). An extensional regime with vertical σ_1 and R$' = $ R, can be sub-divided into radial extensive ($0.00 < R' < 0.25$), pure extensive ($0.25 < R' < 0.75$), transtensive (having both extensive and strike-slip shear) ($0.75 < R' < 1.25$). A strike-slip regime with vertical σ_2 and R$' = 2 - $R, can be sub-divided into pure strike-slip ($1.25 < R' < 1.75$), transpressive (involve both strike-slip and compressive shear) ($1.75 <$

$R' < 2.25$). A compressive regime with σ_3 vertical and $R' = 2 + R$, can be sub-divided into pure compressive ($2.25 < R' < 2.75$) and radial compressive regime ($2.75 < R' < 3.00$).

3.1.3. T-Tecto

The Classical RDM is in-built in T-Tecto studio X5 (Zalohar and Vrabec, 2007), which was used in this work. The working of this method has been described earlier in this section. Parameter D is similar to stress ratio (R) defined by Delvaux et al. (1997).

3.1.4. FaultKin

FaultKin (v.8.0) (Marrett and Allmendinger, 1990; Allmendinger et al., 2012) uses the Linked Bingham distribution statistics function to calculate the average orientation of contractional and extensional axes for the given fault-slip data.

3.1.5. SG2PS (structural geology to post script)

The fault-slip data were inverted in SG2PS (Sasvári and Baharev, 2014) using the methodology of Angelier (1990).

Using the aforementioned programmes, in order to reduce the divergence between the shear stress and measured slip on fault plane and to obtain the best-fit stress tensor solution, we adopted the minimization criterion. It represents a measure of quality of the derived paleostress tensor (Federico et al., 2014). So as to achieve this, the angular difference between the predicted and real slip called the 'misfit

angle' was kept $\leq 20°$ in the present work (Tranos, 2017). All the fault-slip data with a misfit angle $> 20°$ were discarded and the optimum solution was achieved (Delvaux and Sperner, 2003).

3.1.6. Slickenside kinematic indicators

As the fault planes are exposed in uniform lithology, the sense of slip cannot be determined due to lack of any offset markers. In such cases, we inferred the slip-sense solely by observing various slickenside kinematic indicators following the detail works of Doblas et al. (1997), Doblas (1998) and Petit (1987) (Fig. S1, Table S1). Multiple types of kinematic indicators were noted from the fault plane at each site in order to assure the sense of slip. V-shaped crescentic markings include debris trails, sheltering trails, carrot-shaped gouging-grain grooves (Doblas, 1998) (Fig. S1, Table S1). Mineral steps include fault plane asperities (or spurs), quartz crystal fibers, knobby elevations, detached and trailed fragments and tension gashes sub-perpendicular to orientation of striations (Doblas et al., 1997; Doblas, 1998). Nearly all fault planes follow the positive smoothness criteria (i.e., smoothness feels in the direction of motion of missing block) with few follow negative smoothness criteria. Linear, pipe-shaped and v-shaped gouging-grain grooves generated due to trailed material were also observed (Doblas, 1998) (Fig. S1, Table S1). Asymmetric depressions due to removed fault plane material during frictional movement were also observed (Doblas, 1998). Trains of inclined planar structures include domino-style offsetting in tilted blocks exposed in either the footwall or hangingwall; multiple, secondary,
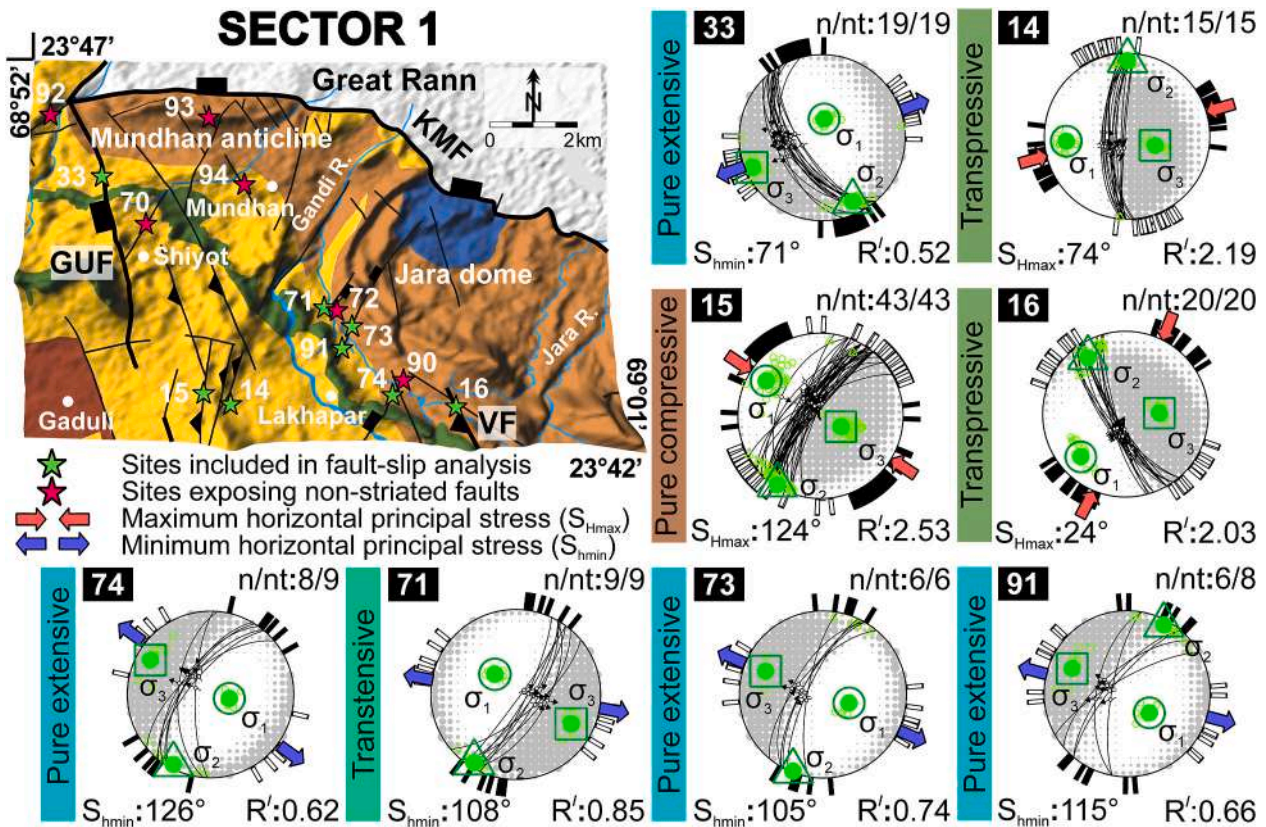

Fig. 3. Structural map of sector 1 (location shown in the geological map of study area in Fig. 2). The sites of fault-slip measurements are marked by green stars. The sites exposing non-striated faults are marked by red stars and are not included in fault-slip analysis. Follow Fig. 2 for interpretation of colors related to lithology shown in the structural map. The stress tensors (lower hemisphere, equal-area projection) deduced by Right Dihedral Method (RDM) implemented in Win_Tensor (Delvaux and Sperner, 2003) for respective sites are shown. Black lines: fault planes with slip vectors (marked by open circles with arrows). Red inward-pointed and blue outward-pointed double arrows: orientation of maximum (S_{Hmax}) and minimum (S_{hmin}) horizontal principal stress respectively. Green circle, triangle and square: orientation of maximum (σ_1), intermediate (σ_2) and minimum (σ_3) stress axes respectively ($\sigma_1 \geq \sigma_2 \geq \sigma_3$). Black solid bars and open bars at the periphery of paleostress tensors: orientation of S_{Hmax} and S_{hmin} axes respectively, for individual fault-slip data. For normal faults, $S_{hmin} = \sigma_3$ and for reverse faults, $S_{Hmax} = \sigma_1$. Site numbers are shown on upper left of stereoplots. n/nt: ratio of number of fault-slip data used in paleostress analysis relative to the total number of fault-slip data collected from the specific site. R': stress index (Delvaux et al., 1997). Counting grid: the white and grey quadrants of the stereoplots corresponding to regions of compression and tension respectively. The colored panels (see Fig. 15 for interpretation of colors) on left of each stereoplots represent the inferred stress regime.
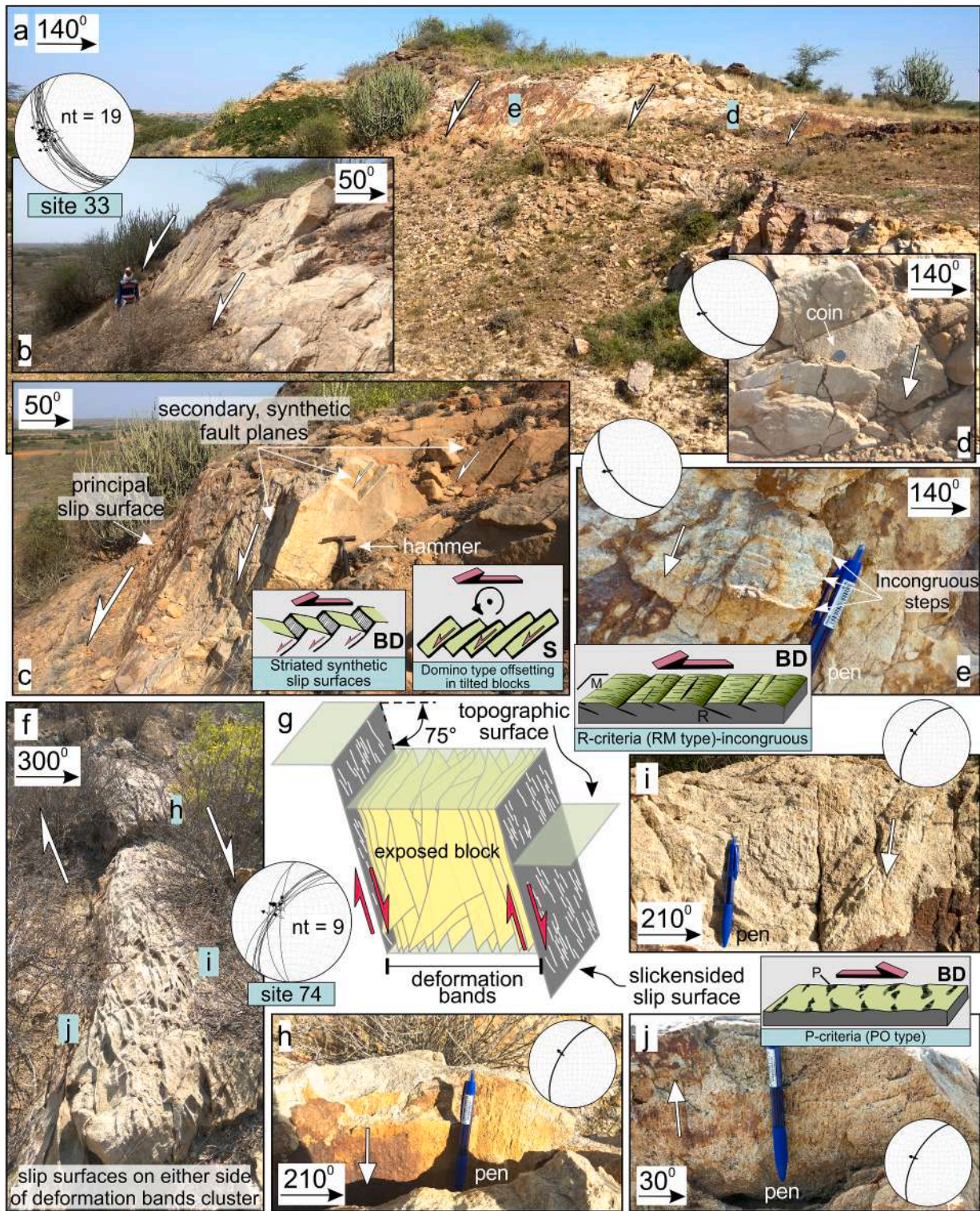
Fig. 4. (a)–(e) NW striking GUF with normal slip exposed at site 33 (sector 1) and (f)–(j) NNE striking cluster of deformation bands exposed along with the striated slip surfaces on both sides, at site 74 (sector 1). See the structural map in Fig. 3 for site location. (a) Panoramic-view of the GUF. d and e denote location of close-ups shown in Figs. (d) and (e). (b) NW looking outcrop-view of the GUF. Height of the person is 188 cm as a scale. (c) Close-view of the exposed footwall shows both the principal slip plane and synthetic, striated slip planes. Length of hammer: 30 cm as scale. (d) and (e) NE looking, close-ups of striated fault plane (attitude: 140° strike, 230° dip direction, 57° dip and lineations attitude: 113° and 110° rake, 48° and 55° plunge, 189° and 203° azimuth). (f) Outcrop-view of deformation bands cluster. h to j show location of close-ups of striated slip planes. (g) The block diagram shows cluster of deformation bands (variably dipping yellow planes) bounded on either sides by striated slip planes (grey colored striated planes). The green horizontal planes show level of topographic surfaces. (h)–(j) The striated fault plane (attitude: 210–230° strike, 300–320° dip direction, 60–70° dip amount and lineations attitude: 93–99° rake, 60–69° plunge, 313–339° azimuth). 13.5 cm long pen as scale in Figs. (e), (h)–(j). Inset sketches: block diagram (BD) of striated synthetic slip surfaces, sectional- (s-) view of domino-type offsetting in tilted blocks in Fig. (c) – modified after fig. 1 of Doblas (1998); BD of RM structures in Fig. (e), PO structures in Fig. (j) – modified after fig. 1e and f of Petit (1987). The white arrows indicate movement of the missing block.

synthetic, striated slip surfaces associated with the principal, striated slip surface. Drag effect of planar elements includes normal and reverse drag. These features are associated with the principal slip surface. They were also used to decode the slip-sense (Doblas, 1998; Mukherjee, 2014). Secondary fractures with diverse morphological variation developed on the fault plane, for example, those following the T-criteria (riedel shear fractures): tensile and crescentic fractures; R-criteria (secondary, synthetic, striated, shear fractures of R orientation): RO-type, RM-type and lunate fractures; P-criteria (secondary, striated, shear fractures of P orientation): PT-type and PO-type were found useful (Petit, 1987) (Fig. S1, Table S1). The morphology of each of the slickenside kinematic indicator is discussed in detail in the field investigations and fault-slip analysis results Section 4. Table S1 (Supplementary data) summarizes the slickenside kinematic indicators utilized in this study.

3.2. Shallow subsurface geophysical investigations

3.2.1. Ground Penetrating Radar (GPR) survey methodology

2D GPR surveys were carried out with a view to map the continuity of the VF and WVF buried below patchy alluvial cover, to reveal their shallow subsurface nature and to further strengthen our field observations indicating the changing slip-sense. Note that all the four sectors were not worked for GPR surveys. The GPR surveys were carried out at three sites: across the VF *(i)* at site 36 (sector 3), *(ii)* ~110 m SE of site 30

(sector 2) and *(iii)* across the WVF at site 34 (sector 3) (Fig. 2). Follow Section 3 (Supplementary data) for details about GPR data recorded near site 30.

3.2.2. Acquisition of geophysical data

Radargrams were obtained in continuous mode by using shielded monostatic 200 MHz frequency antenna. It provided satisfactory results in terms of both the depth of penetration (6 m near site 30, 7.5 m at site 36 and 8 m at site 34) and resolution required to study the near surface nature of faults. The position of the fault was confirmed by observing the changes in reflector pattern discussed later in the GPR imaging interpretation Section 5. Dielectric constant was kept 7 with time window (range) of 125–150 ns during survey operation. At site 36 (sector 3), VF is protruding from the surrounding cultivated soil surface as a small ~0.5 m high striated fault plane in Bhuj sandstone. 17 m long profile was acquired in N240° direction perpendicular to the NW striking fault (Table 1). At site 34 (sector 3), the NNW striking, ~3 m high WVF is exposed in Bhuj sandstone, cross-cutting the NE flowing Makdawali river. GPR survey was conducted in the riverbed of the Makdawali river, with 15 m long profile in N260° direction (Table 1).

3.2.3. Processing of GPR data

The radargram recorded across the VF at site 36 was severely affected by high frequency snow-like noise. It was prevalent from ~4 m (50 ns) depth to vertically downwards throughout the depth of
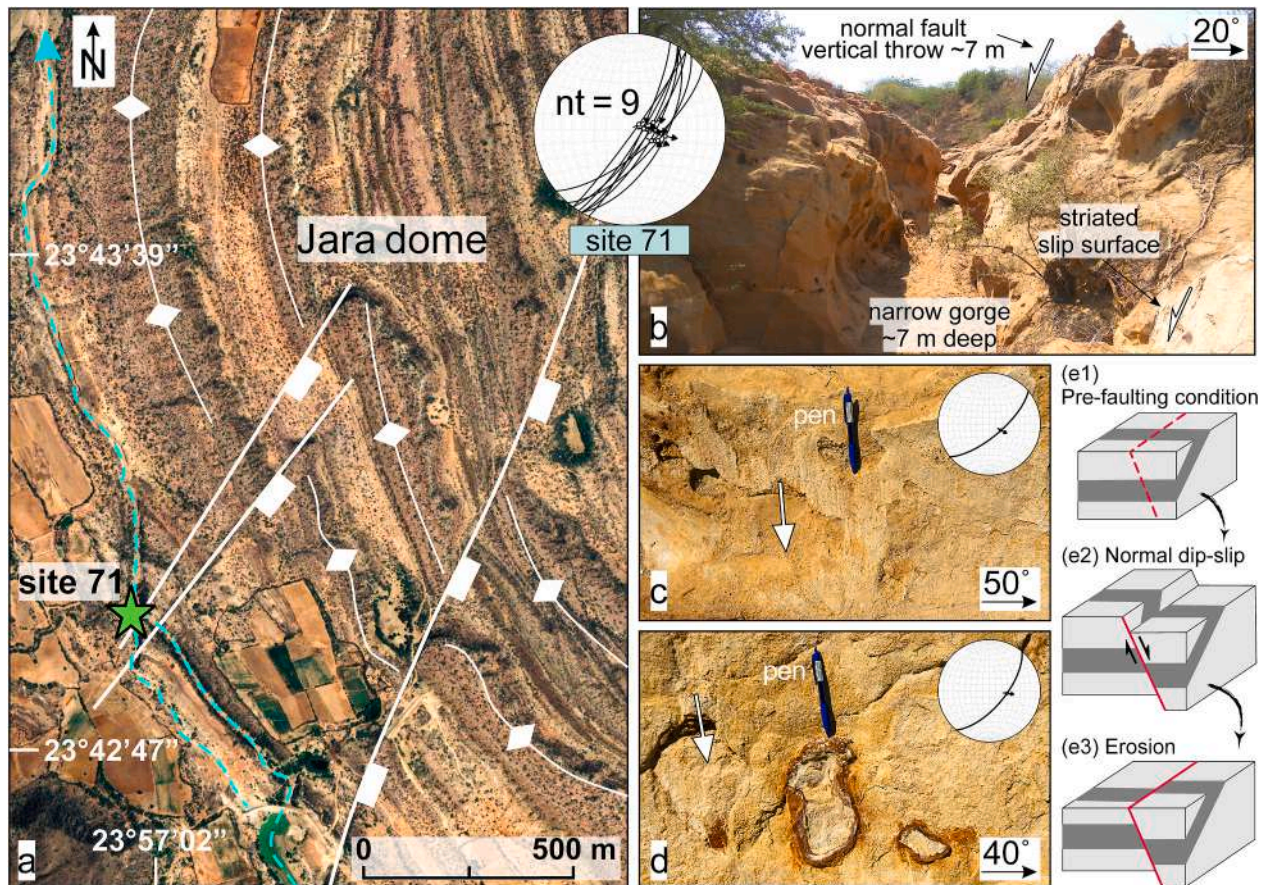

Fig. 5. (a) Annotated Google Earth image – the ridges are marked by white curved lines with rhombus symbols, faults are marked by white, continuous lines with map symbols of normal fault and streams are shown by blue dashed lines with upward arrowhead indicates their northward downstream direction. The NE striking unnamed fault with normal slip exposed in the SW fringe of Jara dome at site 71 (marked by green star) (sector 1, see the structural map in Fig. 3 for site location). (b) West looking view of E striking stream showing ~7 m deep gorge affected on one of its side by the same fault plane with ~7 m vertical throw. (c) and (d) Close-view of the fault plane (attitude: 50° and 40° strike, 140° and 130° dip direction, 70° and 65° dip) with dip-slip striations (attitude: 82° rake, 69° and 64° plunge, 118° and 112° azimuth). 13.5 cm long pen as scale. The white arrows indicate the downward motion of missing hangingwall. (e1)–(e3) Block diagrams (adopted from fig. 30 of Dutta and Mukherjee, 2019) showing activation of pre-existing weak planes as normal fault under extensional stress regime.

radargram (110 ns), masking the real reflections to a great extent. The radargram acquired across the WVF at site 34 was affected by sharp vertical bands of low-frequency. Therefore, processing of raw radargrams was required as the data were affected by different kinds of noises, instability of the equipment and vibrations during survey operations.

The post-survey processing was performed using RADAN (v.7) by GSSI Inc. Full pass background removal filter was applied to suppress the strong low-frequency noise (Geophysical Survey Systems, 2012). Vertical low-pass FIR filter of 400 MHz cut-off frequency was applied for radargram at site 34, which removed frequencies above the established threshold to a great extent (Table 1). Horizontal low-pass smoothing IIR filter of 3–7 scans was then applied to reduce the snow-like noise and to remove the sharp vertical low-frequency bands. Linear range gain was applied to artificially increase the amplitude of radar signals, to offset the attenuation caused during processing described earlier and to improve the visibility of reflectors (Table 1).

Finally, average velocity of 0.14 m ns^{-1} of electro-magnetic (EM) waves was used for time-depth conversion. The average velocity was determined through semblance analysis performed on the common-midpoint (CMP) gather. Using the derived average velocity, migration was performed on radargrams and it produced the most accurate images with significantly less noise.
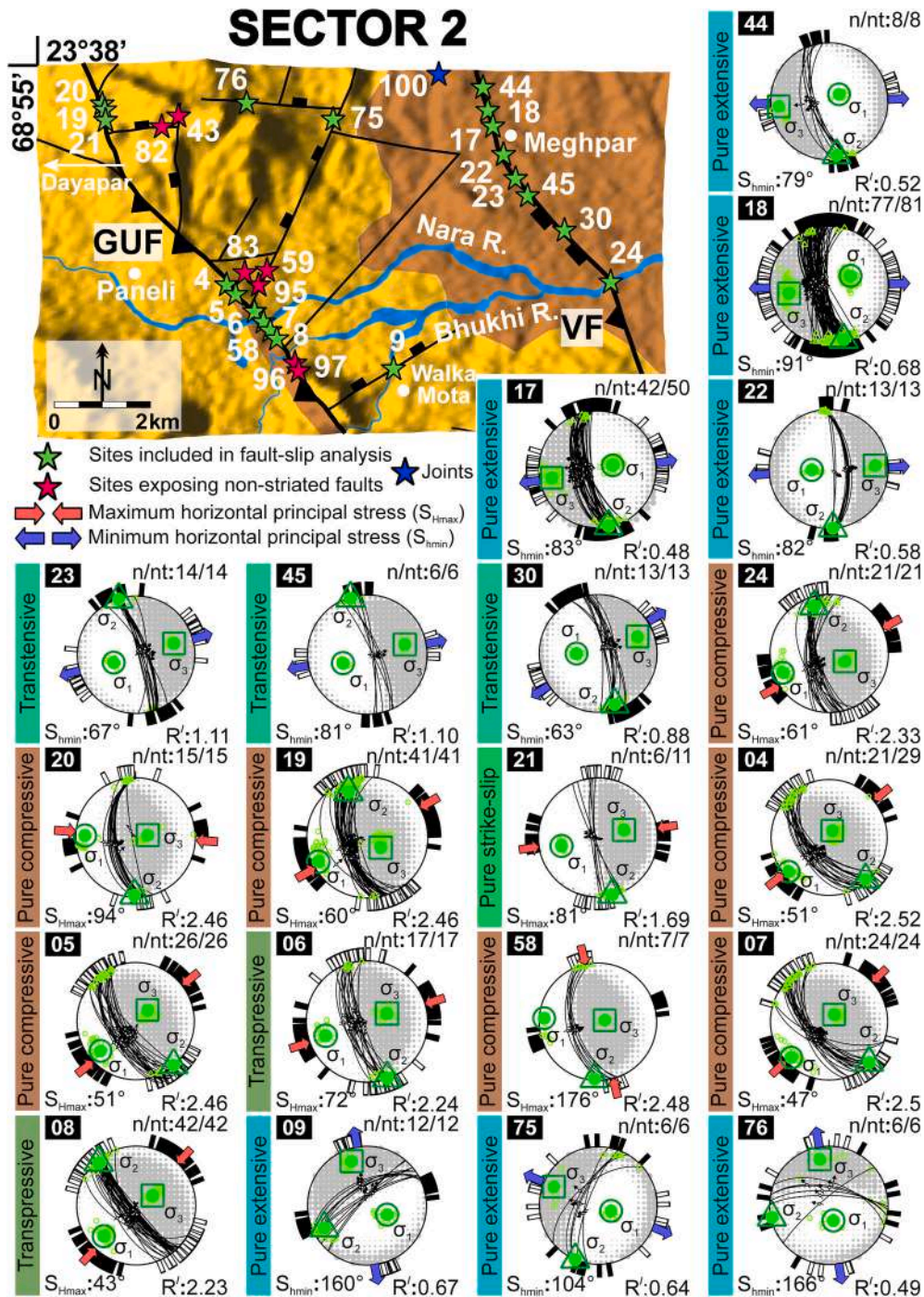
Fig. 6. Structural map of sector 2 (location shown in the geological map of study area in Fig. 2). Follow Fig. 3 caption for interpretation of map and paleostress tensors deduced by Win_Tensor (Delvaux and Sperner, 2003).
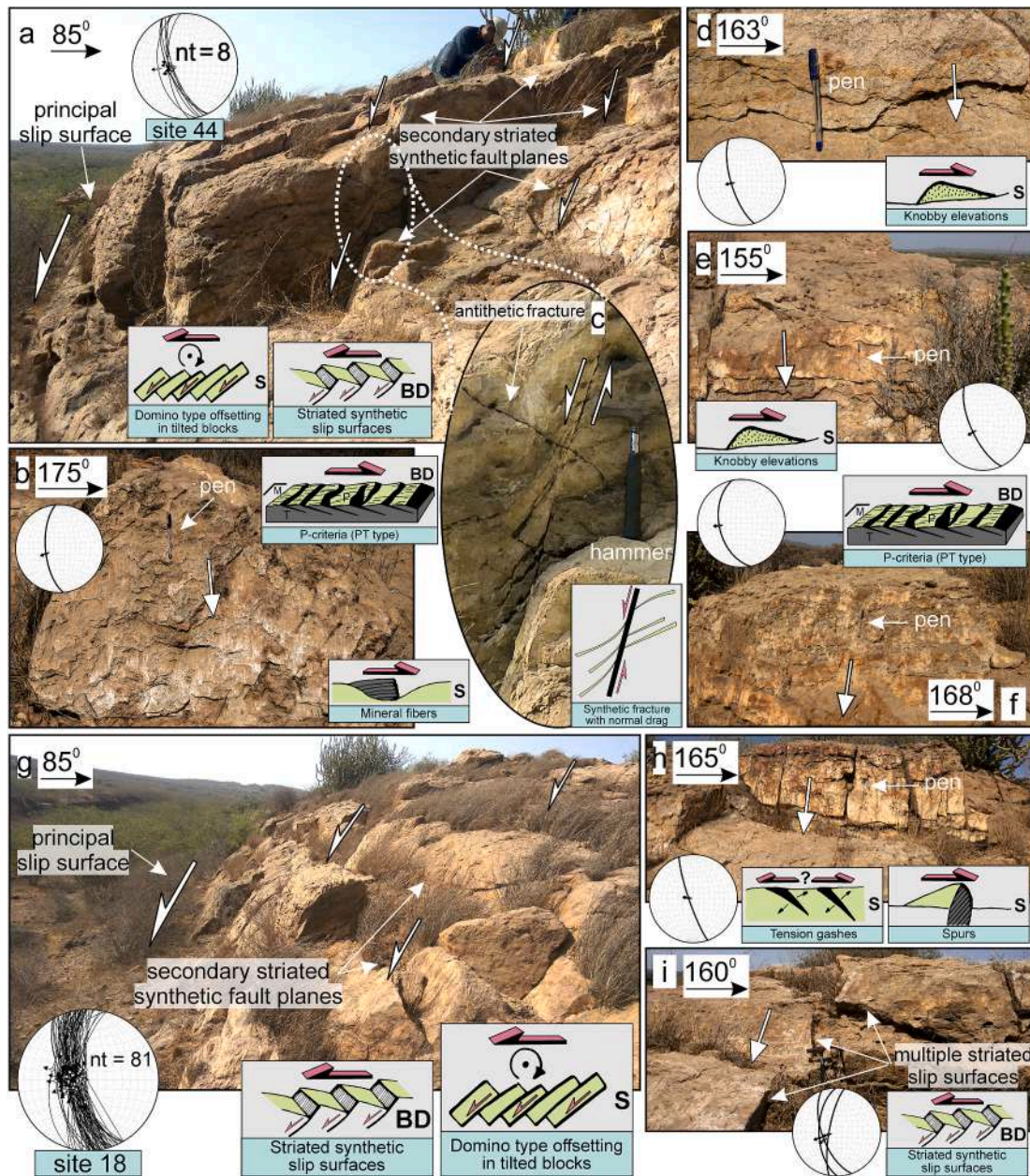
Fig. 7. NNW striking VF with normal slip exposed (a)–(f) at site 44 (sector 2) and (g)–(i) at site 18 (sector 2). See the structural map in Fig. 6 for site location. (a) Multiple, synthetic, striated, secondary slip planes exposed in footwall along with the major slip surface. (b) East looking, close-view of striated fault plane (attitude: 175° strike, 265° dip direction, 64° dip and attitude of lineations: 83° rake, 63° plunge, 249° azimuth). Mineral steps consistently facing down-slope indicate down-slope movement of the missing block. (c) North looking, close-view of a portion of footwall shown as dotted circle in Fig. (a). Length of hammer is 30 cm as scale. (d)–(f) East looking, close-view of the striated fault plane (attitude: 155–168° strike, 245–258° dip direction, 48–71° dip and attitude of lineations: 88–94° rake, 48–71° plunge, 239–264° azimuth). (g) North looking, fault-parallel view of VF. (h) ENE looking, close-view of the striated fault plane (attitude: 161° strike, 251° dip direction, 82° dip and attitude of lineations: 94° rake, 81° plunge, 278° azimuth). The striated fault plane is intensely affected by sub-parallel tension gashes. (i) ENE looking, close-view of multiple striated slip planes (average attitude: 179° strike, 269° dip direction, 57° dip and average attitude of lineations: 80° rake, 56° plunge, 251° azimuth). Inset sketches: sectional- (s-) view of domino-type offsetting in tilted blocks, block diagram (BD) of (sub)-parallel striated, synthetic slip surfaces in Figs. (a), (g) and (i); s-view of mineral fibers in Fig. (b); s-view of knobby elevations in Figs. (d) and (e); s-view of tension gashes and spurs in Fig. (h) – modified after fig. 1 of Doblas (1998). S-view of synthetic fracture with normal drag in Fig. (c). BD of fractures with PT structures in Figs. (b) and (f) – modified after fig. 1 of Petit (1987). 13.5 cm long pen as scale in Figs. (b), (d)–(f) and (h). The white arrows indicate the downward motion of missing hangingwall.

4. Field investigations and fault-slip analysis results

In the VGKNFS, nearly all fault planes of different trends dip steeply (55–88°, few < 55°). NW striking major faults dip uniformly towards SW resembling step-like pattern. Sharp (sub-)vertical steepening of beds of Jhuran and Bhuj sandstones mark the presence of faults. The faults stand out as hard, resistant, positive relief structures against the eroded flat plains and are clearly noticeable from a distance. Straight fault lines

with prominent topographic expression can also be observed in Google Earth Pro imageries (e.g., site 71). This exercise allowed us to define the continuity of major and other unnamed cross-faults. Long, discontinuous, prominent narrow ridges parallel to faults, steep escarpment face and sharp bend of streams are some of the prominent geomorphic expressions that helped in locating the faults. Throw above the ground surface ranges 0.5–30 m. Despite their lower stratigraphic offset than that of E striking uplift-bounding faults, the VGKNFS crops out

discontinuously occurring faults for tens of kms. Along strike, maximum throw is observed around the central part, in Khirasra-Vigodi region, which decreases away towards both the ends of faults and continues as only few m high, discontinuously occurring fault plane above the ground surface.

Each of the sector described earlier comprises variably oriented (NW–NNW, NNE–NE and E) striated and non-striated fault surfaces. *(i)* Northernmost sector 1 (number of collected fault-slip data (nt) = 129) comprises 08 sites, which are included in fault-slip analysis. The sites are located at northern extremity of NW striking GUF, VF; and also other NE, NNE and NW striking unnamed faults originating in the NHRFZ (from Mundhan anticline, Jara dome and inter-domal saddle region in between these two structural domes). *(ii)* South of the Haroda pluton, sector 2 (nt = 463) is located, far away from the influence of NHRFZ. 21 sites are included in fault-slip analysis from sector 2. NW striking GUF; NE, NNE and E striking unnamed faults mostly terminating in the deformation zone of GUF are exposed in sector 2. Also included is the NNW striking rotational VF with anticlockwise rotation of the fault plane (dip direction changing from SW to NE). Fault-slip data are collected from both SW and NE dipping VF. *(iii)* Sector 3 (nt = 443) includes 29 sites exposing NW striking GUF and VF, and NNW striking WVF. NW, NE, E striking, striated/non-striated, unnamed faults and deformation band faults are also exposed in sector 3. *(iv)* From W to E, sector 4 (nt = 115) includes 08 sites exposing NW striking NF; southernmost extremity of NW–NNW striking GUF; bifurcations of the GUF: NW striking NKHF and NNW striking KF. Further E, NW striking VF; and few NW, NNW and E striking unnamed non-striated faults are exposed. VF and GUF are exposed in all the four sectors; WVF is exposed in sectors 3 and 4; NKHF and KF in sector 4 only; and NF in sectors 3 and 4 (Fig. 2).

Mostly dip-slip striations were observed at almost all the sites, which essentially mark normal/reverse slip. Fault planes exposing striations with horizontal/sub-horizontal plunge that record dextral or sinistral slip were scanty. Therefore, fault-slip data indicating strike-slip motion were not included in paleostress analysis. Total 100 sites were explored where fault planes are exposed, out of which 66 sites (including one with systematic joints) were incorporated in paleostress analysis. The remaining 34 sites consist of non-striated fault surfaces were excluded from fault-slip analysis (Table 2).

In VGKNFS, most of the faults show plastered, polished, corrugated and slickensided slip planes affected by (sub-)parallel or conjugate shear fractures. However, at few sites, fault planes are covered by dense, hard, dark reddish ferruginous fault gouge or breccia. No striated slip surface was observed at such sites. Non-striated faults (sense-only data), faults with poor slickenside lineations and unknown slip-sense (line-only data) – fall under the not sure category of fault-slip data (Yamaji and Sato, 2019). Although, paleostress analysis programmes provide handling of such dataset, they were not included in the analysis (Sperner and Zweigel, 2010). Only faults with known or confidently inferred slip-sense were incorporated. Few sites (e.g., site 4 along GUF and site 44 along VF) show development of quartz slickenfibers indicating creep along the fault plane. The faults were studied in vertical/oblique-sections, in the vicinity of anticlines and synclines, sometimes exposed in the riverbed or on a relatively flat topography.

4.1. Sector 1

Two major structures: the Mundhan anticline and Jara dome are exposed in sector 1, generated due to periodic tectonic movement along W–NW striking KMF (Fig. 3). The NW end of VGKNFS is exposed in sector 1 where the identity of NW striking major faults is lost among NW and NE striking discontinuous faults across the Mundhan anticline and Jara dome (Figs. 2 and 3). Node and branch topology network in map-view can be very well expressed as NW striking faults are the younger ones and more extensive that truncate the pre-existing NE striking faults forming characteristic Y-pattern (Morley and Nixon, 2016). In the northernmost extremity, both, NW and NE striking faults disappear in

the deformation zone of the KMF (Fig. 3).

4.1.1. Vigodi Fault (VF) with reverse slip

NW striking and SW dipping VF is encountered in Jhuran sandstone at site 16 (sector 1, Fig. 3). The site crops out the northernmost exposure of VF. Further NW, the fault dies out in the SW fringe of Jara dome. It does not pass through the E-W striking Jaramara scarp located south of Jara dome. Fault-slip analysis results indicate that the VF at site 16 has experienced reverse slip with NE oriented fault-perpendicular shortening (Table 2).

4.1.2. Gugriana Fault (GUF) with oblique-slip

In sector 1, NW striking GUF crops out only at site 33, ~2 km south of western flank of the Mundhan anticline (Fig. 3). The present site witnesses the northernmost occurrence of GUF in Bhuj sandstone. Further north, the fault disappears in the damage zone of KMF. GUF may be a branch of the KMF. Further field investigations are required to verify this statement. Strike of the KMF changes from NW–W where the GUF meets the KMF. Thus, GUF at site 33 (sector 1) acts as a transverse fault and is responsible for the change in strike of the KMF. Because of the tectonic movement along GUF, ENE striking, ~3.3 km long, linear ridge got truncated abruptly on its western end, from where the fault passes and generated a valley locally in the hangingwall side of the fault (Fig. 4a).

Slip-sense is determined by observing the following kinematic indicators: *(i)* development of the secondary, synthetic, striated fault planes; bounding the tilted blocks in the footwall indicate domino-style deformation. Along with the principal slip surface, secondary slip planes have experienced downdip movement (Fig. 4c) (Doblas, 1998), and *(ii)* incongruous fracture steps have been worn by friction during fault movement. These are associated with the negative smoothness criterion (Angelier, 1994) and suggest normal slip. They are arranged in the direction opposite to movement of missing hangingwall and near-perpendicular to striations (Fig. 4e). The steps are of RM-type described by Petit (1987) wherein the main fault plane (/mean fault plane/M surface) is fully striated. R fractures are clearly visible at the tip of dihedron formed by intersection of R and M surfaces. It is noteworthy that the R fractures are closely-spaced, exposed only in a small patch and dipping at low-angle in the M surface.

Paleostress analysis results indicate that the GUF at site 33 (sector 1) has experienced oblique-slip with dominant normal dip-slip and minor dextral strike-slip components, related to pure extensional stress regime with N71° striking S_{hmin} (Table 2). The paleostress tensors generated by T-Tecto, FaultKin and SG2PS programmes are shown in Figs. S2, S3 and S4 respectively (Supplementary data).

4.1.3. Unnamed faults with normal slip

NE striking unnamed cross-faults exposed at sites 71, 73, 74 and 91 show normal slip. NNE striking unnamed faults with reverse slip exposed at sites 14 and 15 are detailed in Section 2.1 (Supplementary data; Fig. S5).

NNE striking unnamed fault is exposed in Jhuran sandstone at site 74 (sector 1; Figs. 3, 4f–j). The fault runs oblique to the VF exposed at site 16. At site 74, NNE striking cluster of deformation bands are observed (Fig. 4f). This cluster is bounded on both the sides by NW dipping, parallel and striated slip planes. Fault-slip data are collected from both the slip surfaces showing normal slip (Fig. 4g). Only the middle segment containing cluster of deformation bands is exposed above the soil surface. Planar, partially striated fault plane shows development of PO structure (of Petit, 1987) on tiny asperities (Fig. 4j). The stoss side of PO structure exhibits striated P surface while lee side do not dip into the fault plane. The P surfaces facing up-slope indicate upward movement of the missing footwall.

A NE striking unnamed fault is encountered in Bhuj Sandstone at the SW fringe of Jara dome (site 71, sector 1; Fig. 3). Two streams merge where the fault cross-cuts (green star in Fig. 5a) and flow northward as a single stream following curvature of the ridge composed of Jhuran
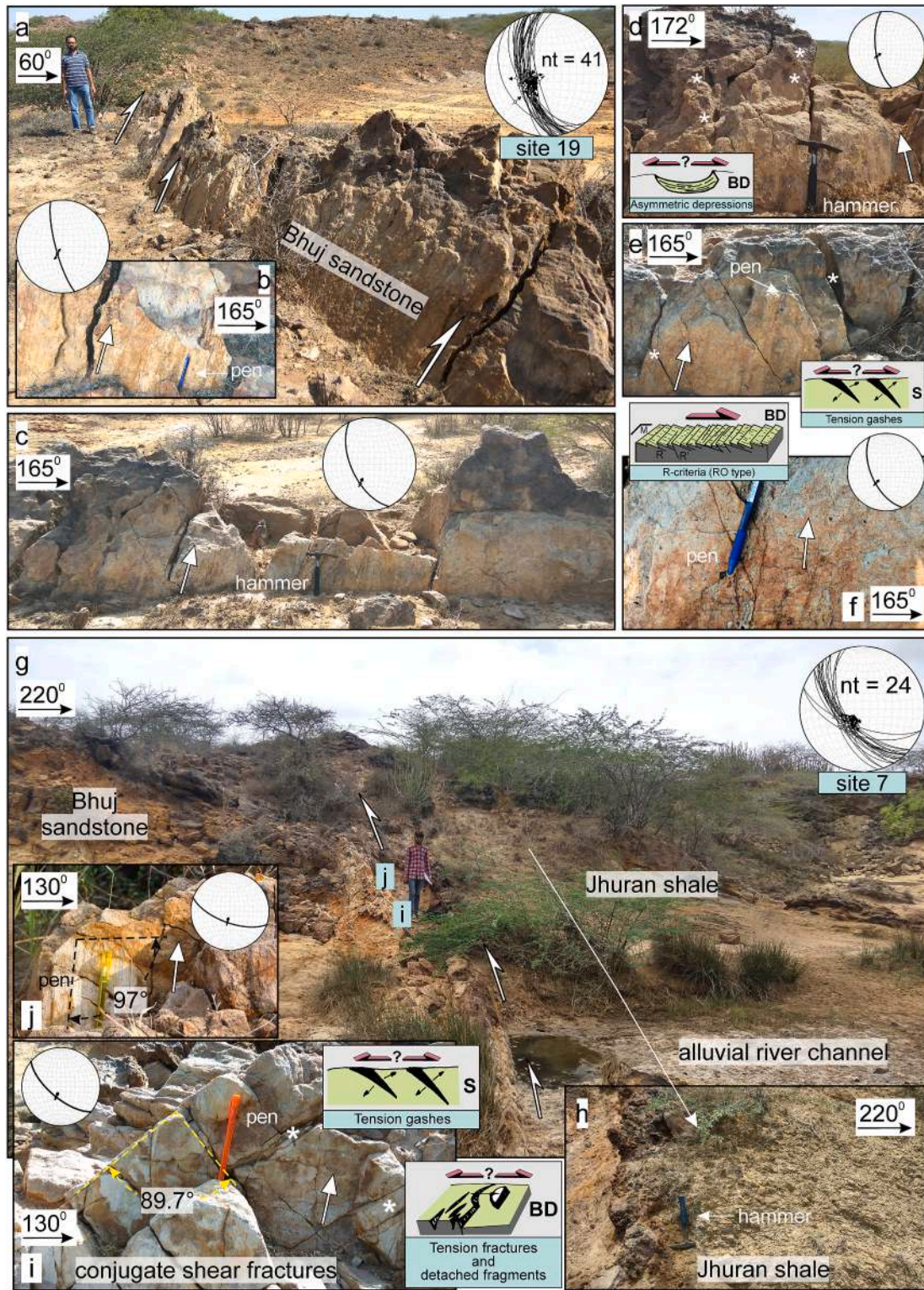
Fig. 8. (a)–(f) NNW striking GUF with reverse slip exposed at site 19 (sector 2) and (g)–(j) NW striking GUF with reverse slip exposed in the cliff section of an alluvial river channel of the NE flowing Khari river, at site 7 (sector 2). See the structural map in Fig. 6 for site location. (a) Outcrop-view of the GUF. Height of the person is 178 cm as scale. (b)–(f) The fault plane (attitude: 155–172° strike, 245–262° dip direction, 59–78° dip) with striations (101–114° rake, 52–76° plunge and 267–288° azimuth). (g) Outcrop-view of the GUF. Height of the person is 188 cm as scale. i and j denote the location of close-ups shown in Figs. (i) and (j). (h) Close-view of the Jhuran shale lithology lying on the hangingwall of SW dipping GUF. (i) and (j) Essentially dip-slip striations (96° and 97° rake, 66° and 60° plunge, 205° and 193° azimuth) developed on a fault plane (attitude: 130° and 110° strike, 220° and 200° dip direction, 67° and 66° dip). A 30 cm long hammer as scale in Figs. (c), (d), (h), and 13.5 cm long pen as a scale in Figs. (b), (e), (f), (i) and (j). Inset sketches: block diagram (BD) of asymmetric depressions in Fig. (d), BD of detached fragments marked by white asterisk in Fig. (i), sectional- (s-) view of tension gashes in Figs. (e) and (i) – reproduced from fig. 1 of Doblas (1998). BD of fractures with RO structures in Fig. (f) – reproduced from fig. 1 of Petit (1987). The white arrows indicate the upward motion of missing hangingwall.
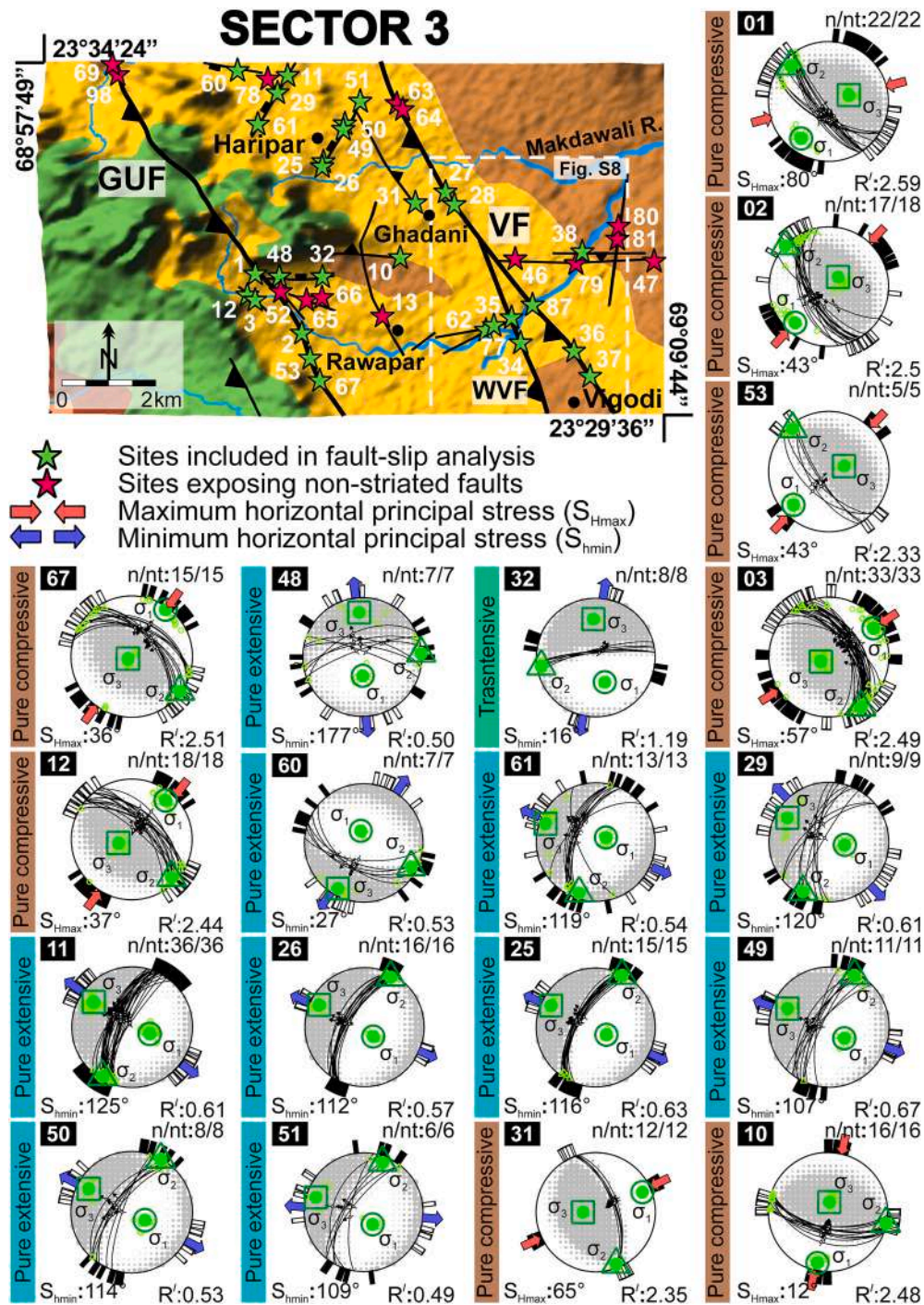
Fig. 9. Structural map of sector 3 (location shown in the geological map of study area in Fig. 2). Follow Fig. 3 caption for interpretation of map and paleostress tensors deduced by Win_Tensor (Delvaux and Sperner, 2003).

sandstone. The fault is exposed on the cliff of an E striking, ~100 m long, ~7 m deep gorge (Fig. 5b). At an outcrop-scale, fault shows normal slip that exhibits dip-slip striations in close-view (Fig. 5c and d). Contrarily, in plan-view, the fault mimics sinistral strike-slip movement and displaces laterally the swerving chain of ridges on SW flank of Jara dome, but that is not the actual case (Fig. 5a). The pre-existing weak plane activated as a normal fault under extensional stress regime and subsequently, erosion occurred in the upthrown block (Fig. 5e1–e3). In another possible case, fault striations developed before folding; rake-angles vary considerably and strike-slip faults become dip-slip (as in Quintà et al., 2012). Looking at the negligible dip of bedding, the

possibility of fault rotation can be ruled out and the condition depicted in Fig. 5(e1)–(e3) seems to be a more plausible explanation.

The fault-slip analysis results indicate that NE striking unnamed faults with normal slip exposed at sites 71, 73, 74 and 91 (sector 1) are related to pure extensive to transtensive stress regime with NW oriented extension (Table 2).

4.2. Sector 2

The investigated sites in sector 2 show dominance of NW–NNW striking VF and GUF, NE striking unnamed faults which terminate
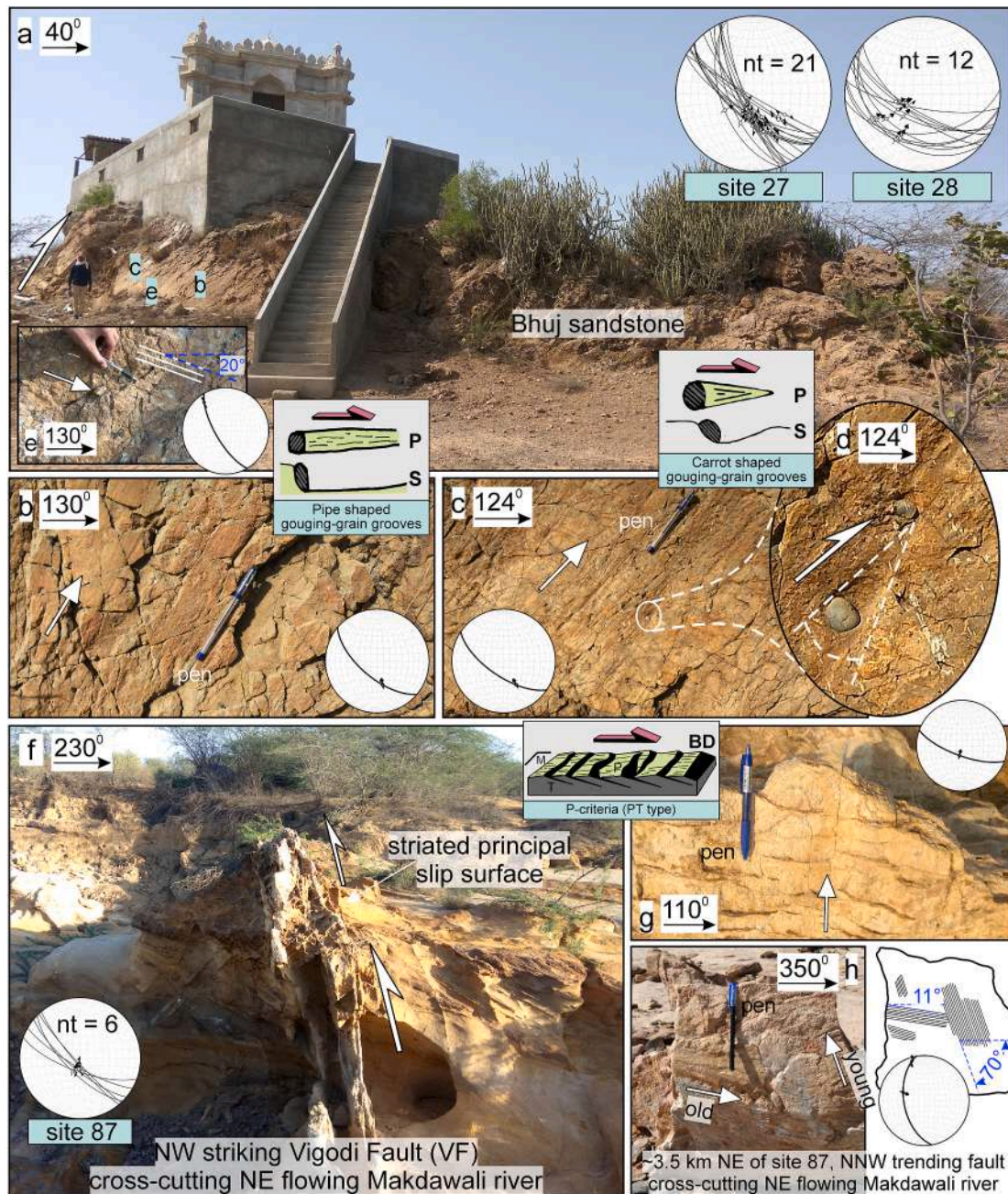
Fig. 10. (a)–(e) NW striking VF with reverse slip at site 27 (sector 3), (f) and (g) NW striking VF with reverse slip cross-cutting NE flowing Makdawali river, at site 87 (sector 3). See the structural map in Fig. 9 for site location. (a) Outcrop-view of the VF. Height of the person is 188 cm as scale. (b) and (c) The striated fault plane (attitude: 130° and 124° strike, 220° and 214° dip direction, 64° and 66° dip, attitude of lineations: 120° and 127° rake, 51° plunge and 167° and 152° azimuth). In close-view, pipe-shaped linear grooves can be observed in Fig. (b). Carrot-shaped grooves can be observed due to dragging effect of grains in Fig. (c). (d) Close-view of carrot-shaped markings shown in Fig. (c). (e) The striated fault plane (attitude: 150° strike, 240° dip direction, 71° dip, attitude of lineations: 20° rake, 19° plunge, 323° azimuth). Location of Figs. (b), (c) and (e) are shown in Fig. (a). (g) The fault plane (attitude: 110° strike, 200° dip direction, 72° dip) with striations (92° rake, 72° plunge, 194° azimuth). (h) Close-up of the fault plane (attitude: 350° strike, 260° dip direction, 53° dip) with two generations of striations (70° and 11° rake, 49° and 09° plunge, 291° and 343° azimuth). 13.8 cm long pen as scale in Figs. (b), (c), (e), (g) and (h). Inset sketches: plane- (p-) and sectional- (s-) view of pipe-shaped and carrot-shaped gouging-grain grooves in Figs. (b) and (c) respectively – modified after fig. 1 of Doblas (1998). Block diagram (BD) of PT type fractures in Fig. (g) – modified after fig. 1f of Petit (1987). The white arrows indicate the motion of missing hangingwall.

against the VF and GUF, and few E striking, high-angle, oblique-slip faults (Fig. 6).

4.2.1. Vigodi Fault (VF) with changing slip-sense

South of the Haroda Pluton, the SW dipping VF is exposed in Jhuran sandstone at sites 44, 18 and 17 (sector 2) in the form of ~1.5 km long, narrow, asymmetric, ~10 m high hill (Fig. 7). We believe ~10 m elevation of the hill is the estimate of surficial throw along the fault. The

surficial throw abruptly decreases at sites 22, 23, 45 and 30 (sector 2) where 30–50 cm high striated fault plane crops out from the surrounding flat soil surface (Fig. S6).

Sites 44 and 18 (sector 2) are located SSE of the Haroda Pluton (Fig. 7). The kinematic indicators observed are as follows – *(i)* Secondary, synthetic, striated slip surfaces exposed along with the principal slip surface (main fault plane) in the footwall (Fig. 7a, g). Their structural attitude is roughly the same as principal slip surface and suggest
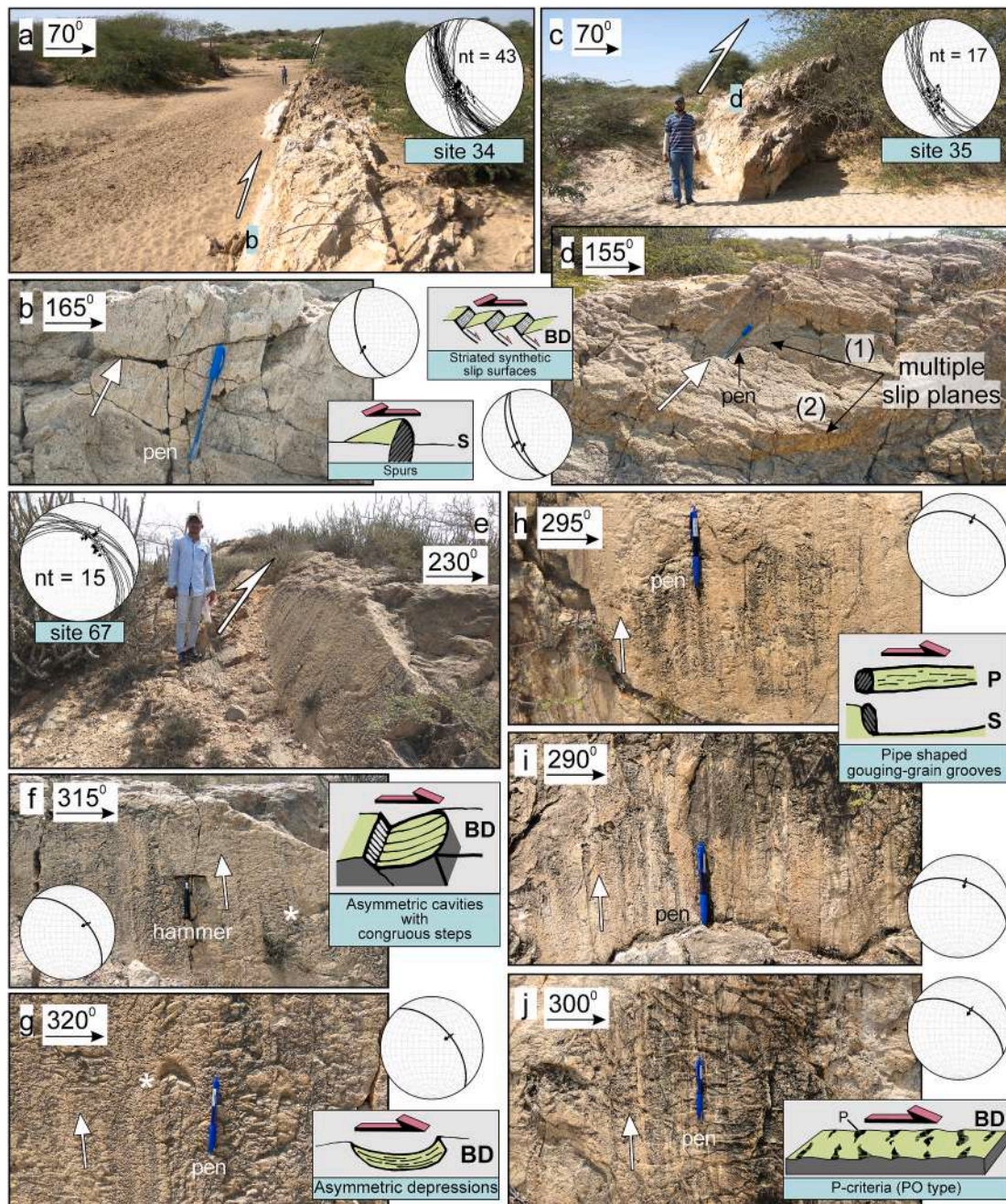
Fig. 11. (a)–(d) NNW striking WVF with reverse slip at sites 34 and 35 (sector 3), and (e)–(j) NW striking GUF with reverse slip exposed at site 67 (sector 3). See the structural map in Fig. 9 for site location. (a) WVF exposed at one of the cliff section of the NE flowing Makdawali river. (b) Close-view of the striated fault plane (attitude: 165° strike, 255° dip direction and 60° dip and attitude of lineations: 115° rake, 52° plunge and 212° azimuth). (c) Fault-parallel view of WVF. Height of the person is 178 cm as scale. (d) Close-view of the two striated fault planes of the same generation. Plane (1) and (2): 158° and 155° strike, 248° and 245° dip direction, 72° and 60° dip, 110° and 97° rake, 63° and 59° plunge, 198° and 231° azimuth. Location of Figs. (b) and (d) are shown in Figs. (a) and (c) respectively. (e) Outcrop-view of the GUF. Height of the person is 188 cm as scale. (f)–(j) The striated fault plane (attitude: 290–320° strike, 25–50° dip direction, 28–55° dip and attitude of lineations: 77–93° rake, 49–55° plunge, 15–67° azimuth). Asymmetric cavity with congruous steps and asymmetric depression facing upslope marked by white asterisk in Figs. (f) and (g) respectively. Figs. (h) and (i) show cm long, linear, pipe-shaped gouging-grains leaving thick black grooves due to their upslope movement on the fault plane. P fractures generated almost perpendicular to striations orientation can be observed in Fig. (j). Inset sketches: sectional-(s-) view of mineral steps (incongruous) in Fig. (b), block diagram (BD) of striated synthetic slip surfaces (incongruous) in Fig. (d), BD of asymmetric cavities with congruous steps in Fig. (f), asymmetric depression in Fig. (g), plane- (p-) and s-view of pipe-shaped gouging-grain grooves in Figs. (h) and (i) – modified after fig. 1 of Doblas (1998). BD of P fractures in Fig. (j) – modified after fig. 1f of Petit (1987). 13.8 cm long pen as scale in Figs. (b), (d), (g)–(j). 30 cm long hammer as scale in Fig. (f). The white arrows indicate the upward motion of missing hangingwall.

domino-style deformation of titled blocks. All the secondary slip surfaces have experienced normal slip. Eight and 81 fault-slip data are recorded from the principal slip surface as well as from the secondary slip surfaces at sites 44 and 18 respectively. *(ii)* Secondary quartz slickenfibers

consistently terminate downslope against the mineral steps (Fig. 7b). The mineral risers step down consistently indicating downslope movement of the missing hangingwall. *(iii)* Crisscrossing, secondary, synthetic and antithetic fractures can be observed (Fig. 7c). The synthetic
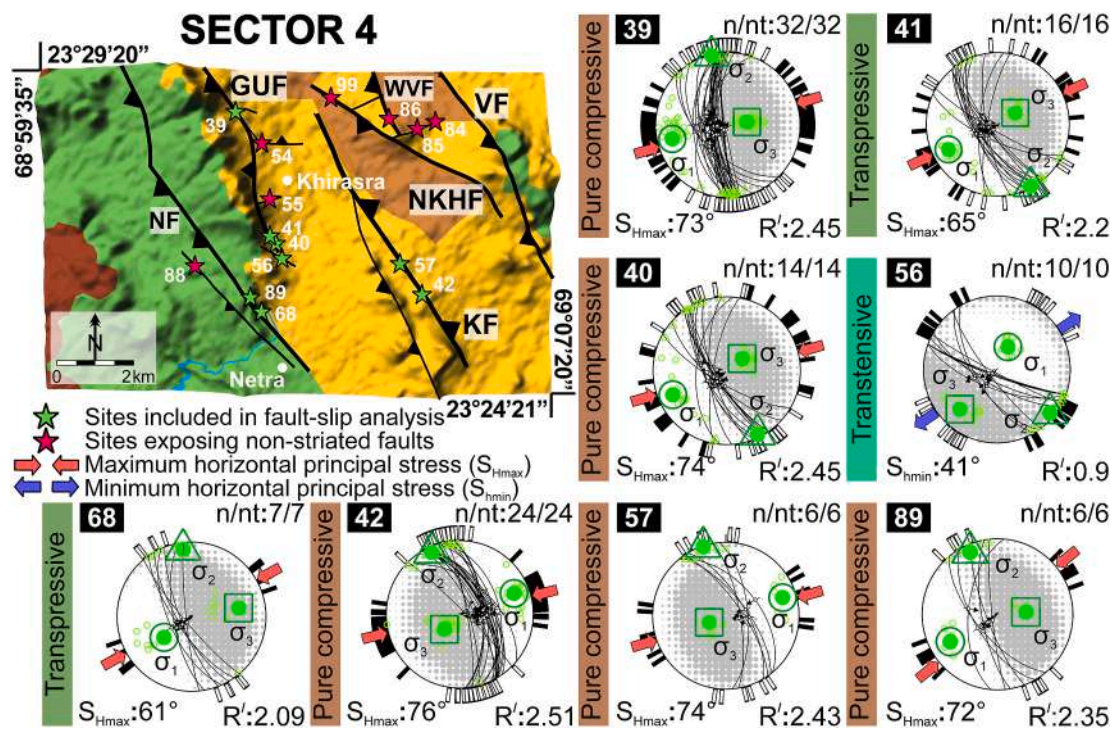
Fig. 12. Structural map of sector 4 (location shown in the geological map of study area in Fig. 2). Follow Fig. 3 caption for interpretation of map and paleostress tensors deduced by Win_Tensor (Delvaux and Sperner, 2003).

fracture shows normal drag fold with round hinge and of dissimilar geometries. Normal drag is inferred as the structural elements in the upthrown side have dragged down. The antithetic fracture does not show any displacement and drag. *(iv)* Knobby asymmetric elevations on the striated fault plane suggest downslope movement of the missing hangingwall (Fig. 7d and e). *(v)* PT structure of Petit (1987) (Fig. 7b, f) are found useful in deciphering normal slip of the VF. M surface is incompletely striated. The striated P surfaces on stoss side of PT structures are prominent and T surfaces are dipping into the M surface at a low angle (Fig. 7b). P surfaces are more developed and striated in Fig. 7b than in Fig. 7f. The intersection of P and T surfaces at the lee side of PT structures has been broken and forms many small steps.

At sites 22, 23, 30 and 45 (sector 2, Fig. 6), normal slip along the NE dipping, ~30–50 cm high, VF has been inferred by observing risers stepping up indicating upward movement of the missing footwall (Fig. S6). N–NE striking sub-vertical joints are exposed in Jhuran sandstone at site 100 (Fig. S7).

The paleostress analysis results indicate that, in the middle segment of the VF, south of Haroda pluton for about 5 km, there has been a shift in stress regime from pure compressive to pure extensive along the strike of the VF. S_{Hmax} strikes N147°–N178° and S_{hmin} strikes N077°–N090° indicating ~N-S compression with R' ranging from 0.48 to 1.11 (Table 2).

4.2.2. Gugriana Fault (GUF) with reverse slip

In sector 2, the GUF is exposed at sites 4, 5, 6, 58, 7, 8 and acts as a lithotectonic contact between Jhuran shale in the hangingwall (partially exposed) and Bhuj sandstone (well-exposed) in the footwall (Fig. 6). NNW striking GUF exposed at sites 19, 20 and 21 in Bhuj sandstone is devoid of Jhuran sandstone/shale in the hangingwall (Fig. 6). In sector 2, the slip-sense along the GUF changes to reverse dip-slip. This is in contrast to the manifestation of GUF at site 33 (~13 km NW of site 20) in sector 1 where it shows oblique-slip with dominant normal dip-slip and minor dextral strike-slip components.

~1 m high fault plane exposed in Bhuj sandstone crops out from the surrounding flat soil surface at site 19 (Sector 2; Fig. 8a–f). The kinematic indicators observed are – *(i)* The risers of asymmetric cavities found on the striated fault surface neither face up-slope nor down-slope in order to determine the slip-sense (Fig. 8d). *(ii)* Parallel to sub-parallel tension gashes oriented parallel/oblique to striations in plan-view of the fault can be observed (Fig. 8e). The slip-sense can only be inferred when tension gashes are observed in sectional-view (s-view in the inset sketch, fig. 1 (1/FR: Fractures) of Doblas, 1998). We could not observe any uniformity in dip of tension gashes in s-view and therefore, it could not be confirmed whether the tension gashes dip in the direction of movement of the missing block. *(iii)* Reverse slip is inferred from RO structures of Petit (1987) (Fig. 8f). The tiny R shears dip at low-angle into the fault plane. The distance between them is very small and regular. M surface appears to be serrated in cross-sectional view.

Site 7 (sector 2) exposes the GUF in the NE flowing tributary of the Nara river (Figs. 6, 8g–j). The river here takes a sub-circular rhythmic turn due to deflection in river course on account of faulting. The GUF shows reverse slip as the older Jhuran shale in the hangingwall has come in contact with the younger Bhuj sandstone in the footwall (Fig. 8g and h). The striated fault plane has been affected by conjugate set of tensile fractures (mode I) ranging in dimension up to tens of centimeters (Fig. 8i). Fractures could not be utilized to determine the slip-sense. Reverse slip is supported by positive smoothness criterion.

The fault-slip analysis results indicate that the GUF with reverse slip in sector 2 is related to pure compressive to transpressive stress regime with $R' \approx 2.50$ and NE–E directed compression (Table 2).

4.3. Sector 3

In sector 3, NW striking GUF, and NE, E and SE striking unnamed faults are exposed in Jhuran and Bhuj sandstones (Fig. 9). NW striking VF and NNW striking WVF both serving as lithotectonic contact between Jhuran and Bhuj sandstone are also exposed.

4.3.1. Vigodi Fault (VF) with reverse slip

In sector 3, NW striking VF exposed in Bhuj sandstone is investigated at sites 27, 28, 87, 36 and 37 (Figs. 9 and S8). The fault exposed at site 37
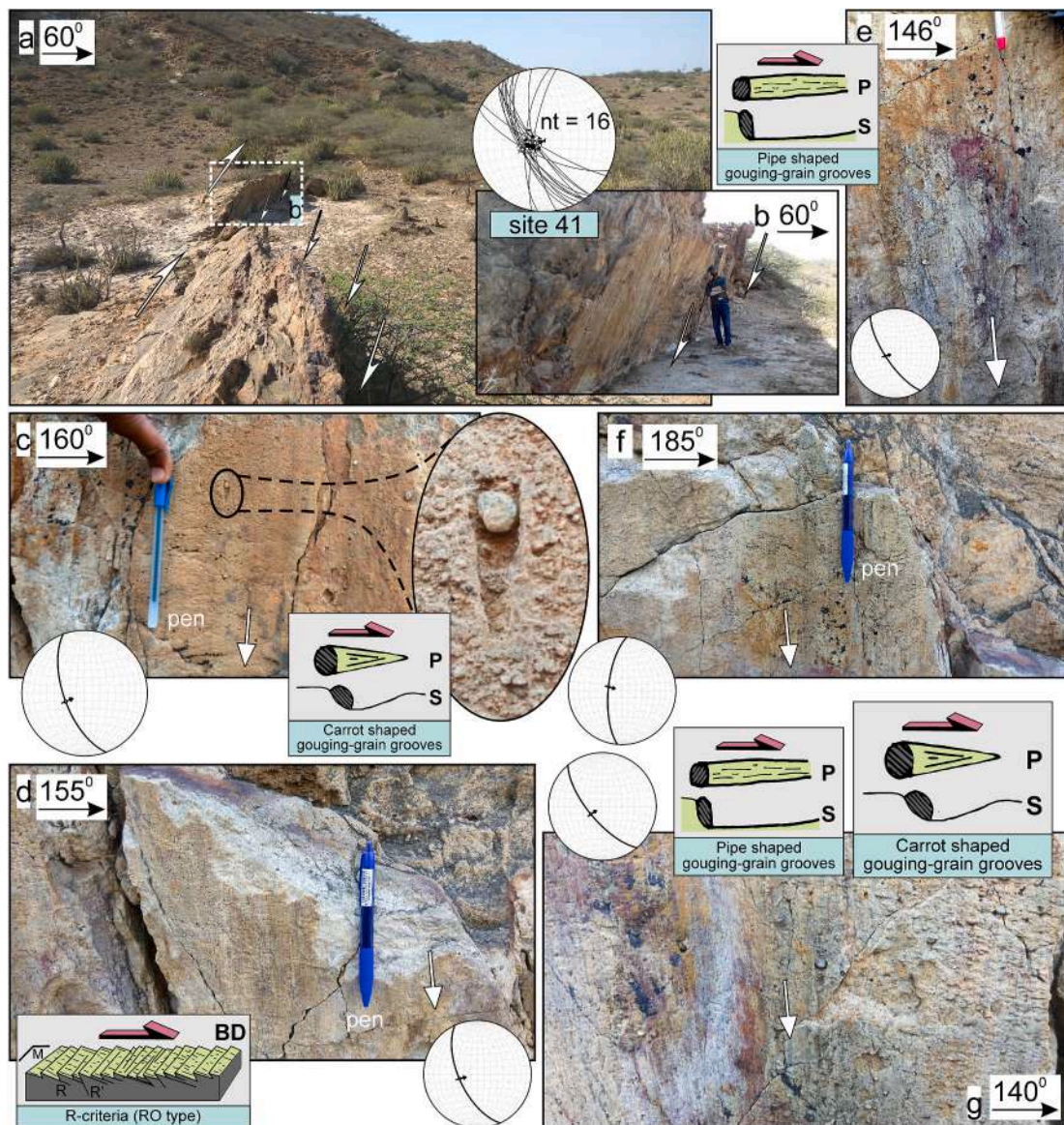
Fig. 13. (a) Panoramic view of NNW striking GUF with reverse slip exposed at site 41 (sector 4, see the structural map in Fig. 12 for site location). (b) NNW looking, fault-parallel view of the GUF. Height of the person is 178 cm as scale. Location of Fig. (b) is shown as white square in Fig. (a). (c)–(g) Close-view of striated fault plane (attitude: 146–185° strike, 250–275° dip direction, 63–72° dip and lineations attitude: 84–92° rake, 63–71° plunge, 246–286° azimuth). Inset sketches: plane-(p-) and sectional- (s-) view of carrot-shaped gouging-grain grooves in Figs. (c), (g) and pipe-shaped gouging-grain grooves in Figs. (e), (g) – modified after fig. 1 of Doblas (1998). Block Diagram (BD) of fractures with RO structures in Fig. (d) – reproduced from fig. 1 of Petit (1987). 13.5 cm long pen as scale in Figs. (c)–(g). The white arrows indicate the motion of missing block.

is detailed in Section 2.3 (Supplementary data; Fig. S9).

Site 27 (sector 3) exposes NW striking, ~3 m high, striated VF (Fig. 10a–e). Site 28 (sector 3) is located ~400 m SE of site 27 (Figs. 9 and S8). The striated fault plane exposes ridge-in-groove lineations (/corrugations). Linear, pipe-shaped gouging grain grooves developed by down-dip movement of protruding grains/clasts indicate upslope movement of the hangingwall (Fig. 10b). Also note the conjugate fractures formed on faulted surface. Carrot-shaped tool marks generated due to gouging effect of the quartz grains dragged down-dip are also visible with the naked eye (Fig. 10c). Acute angle or concavity of the kinematic indicator lies in the upslope motion of the missing hangingwall indicating reverse slip. The only exposure of striated fault plane (20° rake) denoting sinistral strike-slip motion is also observed, which pre-dates the reverse slip (Fig. 10e). Due to unavailability of more such fault planes with strike-slip striations (nt = 3), they are avoided in the analysis.

At site 87 (sector 3), the fault crosses the NE flowing Makdawali river (Figs. 9 and 10f, g). The SW dipping, dense cluster of deformation bands along with the striated, principal slip surface occur in the fault damage zone (Fig. 10f). The striated fault plane shows shear fractures (PT-type) near-perpendicular to the orientation of striations (Fig. 10g). See Fig. 7b description (Section 4.2.1) for details regarding morphology of fractures following the PT-criteria of Petit (1987). ~3.5 km NE of site 87 in sector 3, another NNW striking fault is encountered cross-cutting the NE flowing Makdawali river (Fig. 10h). The fault exposes multiple generations of striations in which the dip-slip striations clearly seem to truncate the striations denoting strike-slip motion. The fault is not included in paleostress analysis due to insufficient number of fault-slip data (nt = 2).

The fault-slip analysis results indicate that the VF with reverse slip exposed in sector 3 is related to pure compressive stress regime with R′ = 1.93–2.52 and NNE–NE directed compression (Table 2).
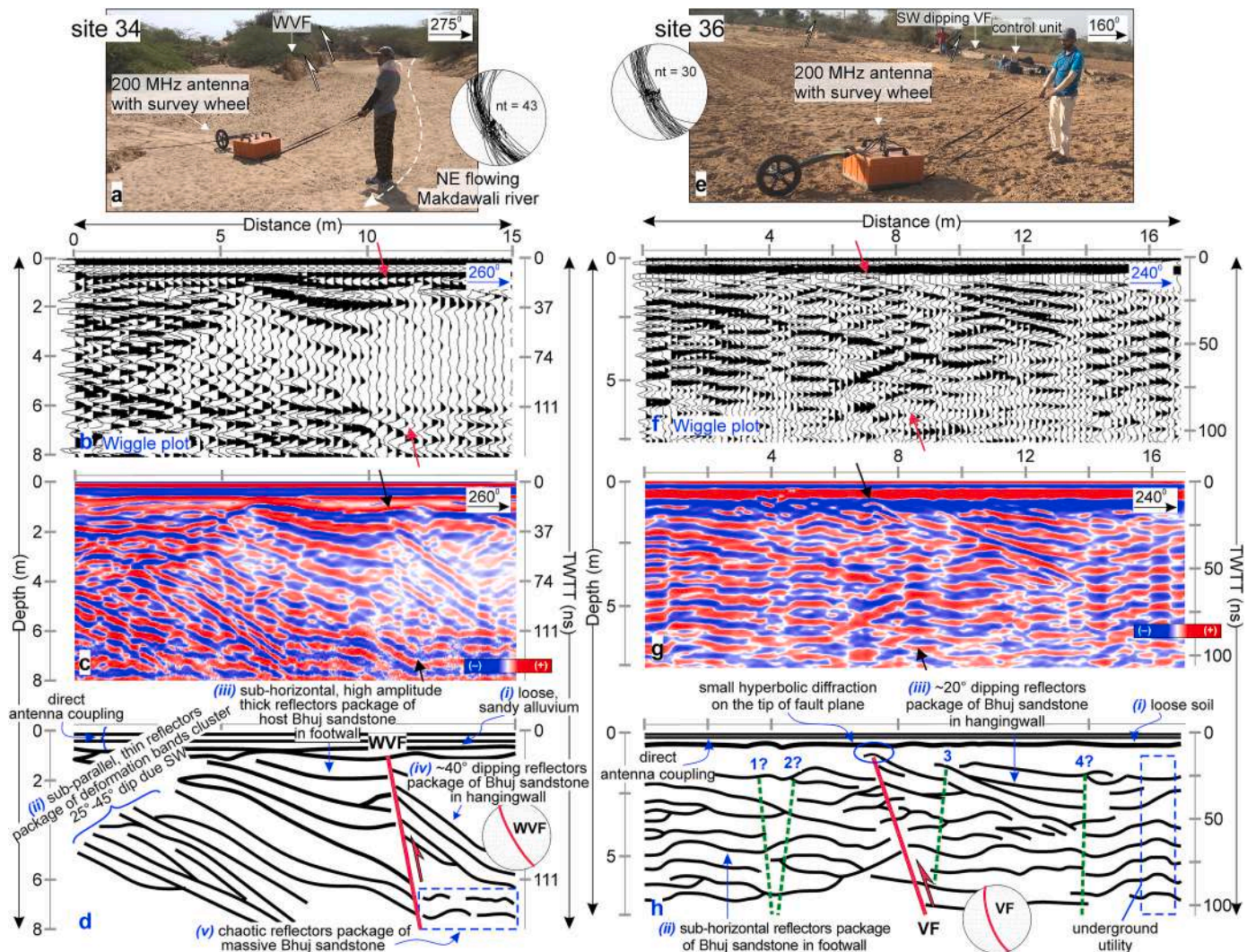
Fig. 14. (a)–(d) 15 m long, SW oriented GPR profile acquired across the NNW striking WVF at site 34 (sector 3). Transect is taken in the riverbed of NE flowing Makdawali river. (e)–(h) 17 m long, SW oriented GPR profile recorded across the NW striking VF at site 36 (sector 3). See geological map of the study area in Fig. 2 for location of GPR survey sites. Axis on left side shows penetration depth in meters and on right side two way travel time (TWTT) in ns is denoted. The upper axis shows profile length in meters. Inset stereonet in Figs. (d) and (h) show the geometry of WVF and VF inferred from the radargram.

4.3.2. West Vigodi Fault (WVF) with reverse slip

At sites 34 and 35 (sector 3), the SW dipping WVF is exposed in Bhuj sandstone at one of the cliff section of NE flowing Makdawali river (Figs. 9 and 11a–d). The Makdawali river has been deflected, where the fault crosses the river (Fig. S8). The two E and NE flowing tributaries meet where the fault passes through, the river then flows towards NE.

The multiple, synthetic, striated slip planes indicate upward movement of the missing hangingwall (Fig. 11d). The rake of lineations goes up to ~135° indicating sinistral strike-slip component is also involved along with the reverse slip. The fault-slip analysis results indicate that the WVF is related to pure compressive stress regime with NE oriented compression (Table 2).

4.3.3. Gugriana Fault (GUF) with reverse slip

The SW dipping, striated GUF exposed in Bhuj sandstone is investigated at sites 1, 2, 53 and 67 (Fig. 9).

At site 67 (sector 3), the NE striking GUF is exposed in Bhuj sandstone (Figs. 9 and 11e–j). SSE of site 2, the dip direction of NW striking GUF changes from SW and dip towards NE (Fig. 11e–j). The slip-sense has been inferred by observing the following kinematic indicators – *(i)* asymmetric cavities (Fig. 11f and g) and *(ii)* linear, pipe-shaped grooves generated due to gouging effect of grains (Fig. 11h and i) indicate

upward movement of the missing hangingwall. *(iii)* P fractures oblique to the orientation of striations are also observed (Fig. 11j). The fault-slip analysis results indicate that the GUF exposed in sector 3 is related to pure compressive stress regime with $R' \approx 2.5$ and NE oriented compression (Table 2).

Follow *(i)* Section 2.4 (Supplementary data) for details about WSW striking deformation band fault (site 62; Fig. S10) with normal slip and NNW striking slipped deformation band (site 77; Fig. S11) with normal slip and, *(ii)* Section 2.5 (Supplementary data) for details about NW striking deformation band fault with reverse slip (site 12; Fig. S12).

4.4. Sector 4

NW striking parallel NF, GUF, NKHF, VF; and NNW striking KF and WVF are exposed in sector 4 (Fig. 12). The NKHF and KF, where the former and northern segment of the later serve as lithotectonic contact between Jhuran and Bhuj sandstone. The NKHF is non-striated and is therefore, not included in the paleostress analysis.

4.4.1. Gugriana Fault (GUF) with reverse slip

The southernmost extremity of NNW–NW striking GUF appears in sector 4. The fault is exposed for ~5 km in Bhuj sandstone with

subsidiary, local occurrence of shale lithology in fault damage zone at sites 39, 40 and 41 (Fig. 12). At site 41 (sector 4), GUF is exposed ~300 m east of the NNW striking asymmetrical hill range with steep eastward and gentler westward slope (Fig. 13). Locally, the fault appears to be of having curved geometry with strike ranging between N140°–N190° E (Fig. 13a). The striated slip surfaces are found on both the sides of the positive relief structure. Carrot-shaped (Fig. 13c, g) and pipe-shaped gouging grain grooves (Fig. 13e, g) are formed due to plucking effect of upward moving grains during fault motion. This indicates a downward movement of the missing footwall. See Fig. 10 description (Section 4.3.1) for details regarding morphology of carrot-shaped and pipe-shaped gouging grain grooves of Doblas (1998). RO-type fractures in Fig. 13d also suggest downward motion of the missing footwall.

The fault-slip analysis results indicate that the GUF with reverse slip exposed in sector 4 is related to pure compressive to transpressive stress regime with R′ ranging 2.20–2.45 and NE oriented compression (Table 2).

4.4.2. Netra Fault (NF) and Khirasra Fault (KF) with reverse slip

Knobby, asymmetric elevations sloping upward observed on striated fault plane indicate upward movement of the missing hangingwall thereby suggesting reverse slip along the NF (Figs. S13a–d). The NNW striking KF, which is a branch of GUF, is exposed at sites 42 and 57 (sector 4; Figs. S13e and f). At both the sites, the fault is exposed on top of a narrow, linear NNW striking fault-controlled hill. Smooth-rough criteria worked well as friction felt downdip suggesting upward movement of the missing hangingwall thereby indicating reverse slip.

The fault-slip analysis results indicate that the NF and KF with reverse slip are related to pure compressive stress regime with R′ ranging 2.09–2.51 and NE oriented compression (Table 2).

5. GPR imaging interpretation

5.1. Site 34 - West Vigodi Fault (WVF)

The processed radargram at site 34 (sector 3) shows SW dipping WVF at ~11 m horizontal distance (Fig. 14a–d). The clear lateral discontinuity of reflectors passing across the fault plane can be observed. The near surface fault geometry and slip-sense inferred from the radargram correlates well with the nearby surficial fault exposure. From NE to SW, thinning of reflectors is observed across the fault plane. The radargram can be divided into five distinct radar reflection packages demarcated based on the reflector pattern response:

(i) Long, continuous, horizontal reflectors

At 0–37 ns depth interval, the top segment is occupied by long, continuous, thick reflectors belonging to loose, sandy alluvium in the riverbed (Fig. 14d).

(ii) Moderate to gently, SW dipping reflectors package in footwall

GPR survey also picked the hard, compacted, cluster of deformation bands (dies out along the fault) as their subtle dielectric contrast with the host, friable Bhuj sandstone (Fig. 14d). The deformation bands cluster is marked by closely-spaced, sub-parallel, thin, 25–45° dipping reflectors, which continue up to 7 m horizontal distance. It has to be noted that each, wavy, undulating reflector pattern within the package may/may not mark the individual strand of deformation bands cluster.

(iii) Sub-horizontal reflectors package in footwall

In the interval of 5–10 m horizontal distance, the amplitude of reflectors suddenly increases. This radar reflection package encompasses the sub-horizontal, high amplitude, thick reflectors of massive, host Bhuj sandstone (devoid of any deformation bands) in the footwall that are

truncated along the SW dipping fault (Fig. 14d).

(iv) SW dipping reflectors package in hangingwall

In the hangingwall, in the interval of 11–15 m horizontal distance, ~40° dipping towards SW, thin reflectors of Bhuj sandstone ride over (displaced upward) the SW dipping/sub-horizontal thick reflectors in the footwall (radar reflectors package (iii)) indicating reverse dip-slip along the fault (Fig. 14d). Along with the sheer change in dip of reflectors across the fault, there is a sudden decrease in the amplitude of radar reflections from reflectors package (iii) to (iv), due to deformation in the damage zone. The low amplitude radar signals can be clearly observed in the wiggle traces (Fig. 14b).

(v) Chaotic radar reflection package

Towards the SW side, in the deeper segment of radargram, a package of thin, small, discontinuous yet (sub-)horizontal reflectors with no specific shape can be observed in the hangingwall block of the WVF between 6 and 8 m depth (110–150 ns depth range) (highlighted in the dashed box area in Fig. 14d).

5.2. Site 36 - Vigodi Fault (VF)

At site 36, the VF can be identified at 7.5 m horizontal distance in the processed radargram. The fault is represented by truncation and offset of continuous reflectors (Fig. 14f–h). At the far side of field photograph in Fig. 14e, the SW dipping fault is exposed with ~0.5 m positive relief from the surrounding flat soil surface. The radargram can be divided into three distinct radar reflection packages:

(i) Thick, long, continuous reflector

At 0–25 ns depth interval, in the uppermost segment, the loose soil is represented by long, continuous, thick reflector (Fig. 14h).

(ii) Sub-horizontal reflectors package in footwall

At 0–7.5 m horizontal distance; long, continuous, horizontal to sub-horizontal reflectors belonging to Bhuj sandstone can be observed in the footwall. They are truncated along the SW dipping fault. The fault is marked as a red continuous line in Fig. 14h.

(iii) Moderately dipping reflectors package in hangingwall

In the upthrown block, the radar reflections with ~20° dip towards SW, belonging to the deformed Bhuj sandstone are identified in the interval of 7.5–14 m horizontal distance. Reverse dip-slip is exemplified as the SW dipping reflectors in the hangingwall are displaced upward with respect to almost horizontal reflectors in the footwall (Fig. 14h). The multiple, green dashed lines represent the possible presence of deformation bands. They are identified by the offset and change in dip of continuous reflectors throughout the depth of profile. Due to the soil cover, their presence is not verified by the surficial exposure except the antithetic band 3. Almost horizontal, high amplitude, thick radar reflections throughout the depth of profile at 16–17 m horizontal distance are due to man-made utility buried underground (Fig. 14h).

The characteristic signatures of locating a fault plane are identified viz., truncation, thinning and dip change of radar reflector facies across the fault plane. Also, small hyperbolic diffraction at the tip of fault plane can be observed at 7.5 m horizontal distance. Thus, the near surface fault geometry and reverse slip-sense inferred from the GPR survey correlates well with the nearby surficial fault exposure. Follow Section 3.3 (Supplementary data) for details about interpretation of GPR data recorded near site 30 across the VF (Fig. S6d).
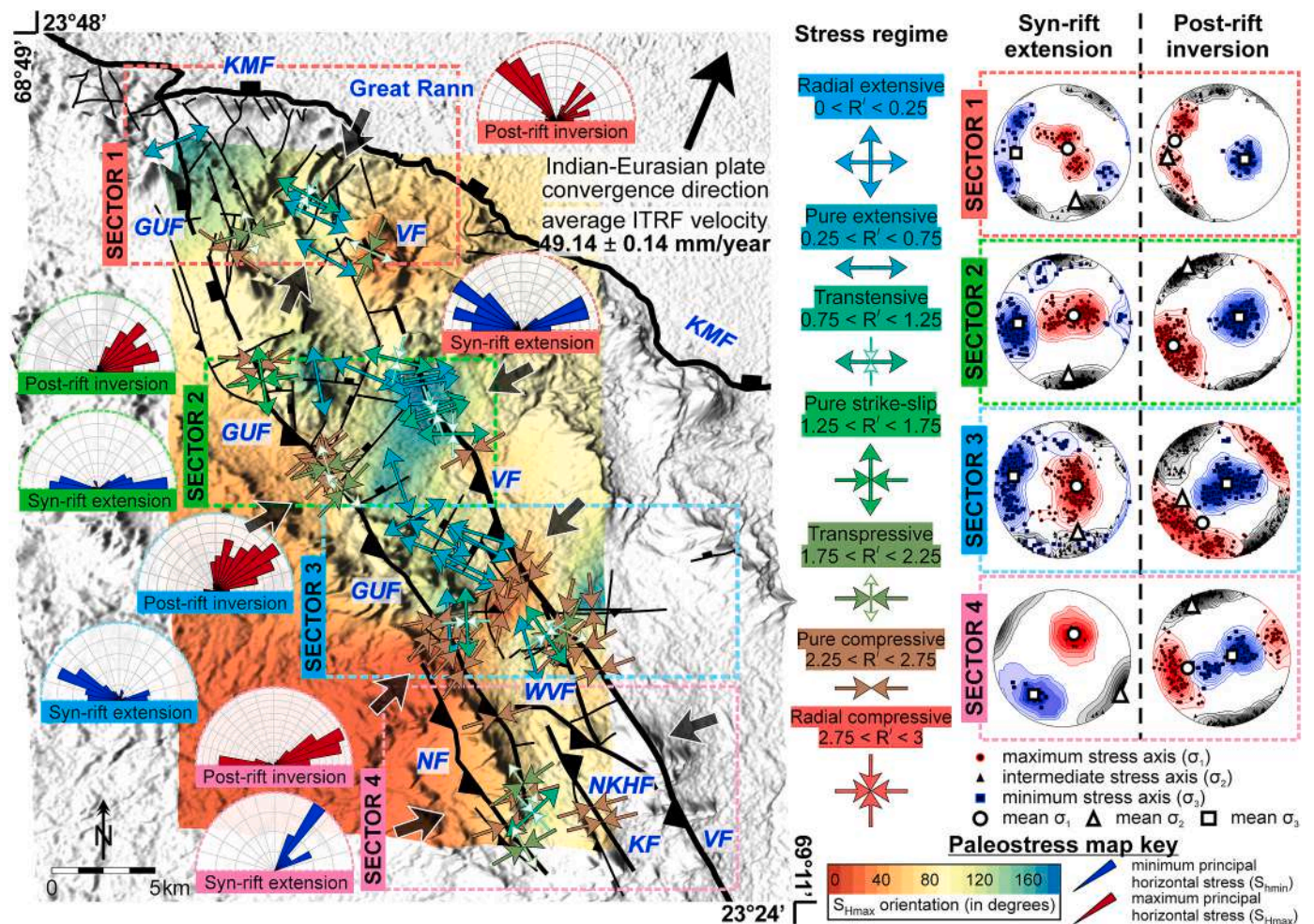
Fig. 15. Regional kinematics of the VGKNFS with reconstruction of the Late Mesozoic to Cenozoic paleostress orientations derived from fault-slip analysis. The biggest black inward-pointed double arrows (at the periphery of each sector) indicate the mean compressional directions derived for each of the four sectors. Inward-pointed and outward-pointed double arrows (within each sector): orientation of S_{Hmax} and S_{hmin} respectively. Colors given to arrows are according to the color scheme shown in vertical column of stress regime. Color scheme is based on the type of stress regime and stress index (R′) (Delvaux et al., 1997). Rose plots show S_{Hmax} (red bars) and S_{hmin} (blue bars) orientation for each of the sector. On the right side of the map are sector-wise distribution of lower hemisphere, equal area projections for syn-rift extension and post-rift inversion phases representing principal stress axes (red circle: σ_1, black triangle: σ_2 and blue square: σ_3) population calculated for each site with kamb contours. The biggest circle, triangle and square in stereonet represent mean σ_1, σ_2 and σ_3 respectively. During syn-rift extension, sector 1: mean σ_1 at 052°∠82°, mean σ_2 at 165°∠25°, mean σ_3 at 270°∠33°; sector 2: mean σ_1 at 056°∠77°; mean σ_2 at 175°∠20°, mean σ_3 at 267°∠32°; sector 3: mean σ_1 at 086°∠75°, mean σ_2 at 161°∠29°, mean σ_3 at 283°∠26°; sector 4: mean σ_1 at 026°∠59°, mean σ_2 at 124°∠03°, mean σ_3 at 216°∠32°. During post-rift inversion, sector 1: mean σ_1 at 282°∠34°, mean σ_2 at 264°∠23°, mean σ_3 at 105°∠60°; sector 2: mean σ_1 at 241°∠22°, mean σ_2 at 326°∠10°, mean σ_3 at 075°∠70°; sector 3: mean σ_1 at 208°∠45°, mean σ_2 at 254°∠43°, mean σ_3 at 046°∠80°; sector 4: mean σ_1 at 254°∠48°, mean σ_2 at 330°∠16°, mean σ_3 at 082°∠77°. The average International Terrestrial Reference Frame (ITRF) velocity in the KRB is after Dumka et al. (2019). The colored overlay draped over shaded relief map represent S_{Hmax} orientation. Warm colors represent NNE–NE oriented S_{Hmax}.

6. Discussion

The neotectonically active KRB has undergone thick-skinned deformation and represent positive basin inversion tectonics. So as to define the major and minor stress fields reliably and to understand the effect of local perturbations in the regional stress field acting upon the VGKNFS, unnamed cross-faults of varying orientations are also included in the paleostress analysis, along with the major NW striking faults.

The VF shows reverse dip-slip in sectors 1, 3 and 4, where the hangingwall on SW side has come up (e.g., Fig. 10). However, in sector 2, south of the Haroda pluton, the slip-sense alters to normal dip-slip (e.g., Fig. 7). Also, in sector 2, the dip direction of VF changes with *(i)* SW dipping fault plane in the northern segment (Fig. 7) which rotates to *(ii)* NE dipping fault plane in the southern segment with abrupt decrease in throw (Fig. S6). However, slip-sense remains the same i.e., normal dip-slip with *(i)* missing hangingwall on SW side of the fault plane has moved down with respect to the exposed footwall in the case of SW

dipping VF whereas *(ii)* missing footwall on SW side has moved up and eroded away with respect to the exposed hangingwall in the case of NE dipping VF. NNW striking WVF bifurcates from the NW striking VF along its northern extremity (in sector 3; Fig. 9) and ends up against the NW striking NKHF along its southern extremity (in sector 4; Fig. 12). The WVF shows oblique-slip with reverse dip-slip and sinistral strike-slip components (Fig. 11a–d).

Comparing the exposure of GUF in all the four sectors, it is observed that the SW–WSW dipping footwall is exposed in sectors 1, 2 and 3 while the hangingwall is missing (Fig. 4a–e). Whereas in sector 4, the SW–WSW dipping hangingwall is exposed and footwall is missing (Fig. 13). The GUF in its NW extremity, in the vicinity of KMF, is characterized by oblique-slip with dominant normal dip-slip and minor dextral strike-slip components (site 33 in sector 1). While in rest of the sectors, GUF shows reverse slip. Thus, the GUF shows along-strike change in slip-sense. Furthermore, change in the orientation of slickenside lineations along the strike of GUF has been observed. At its
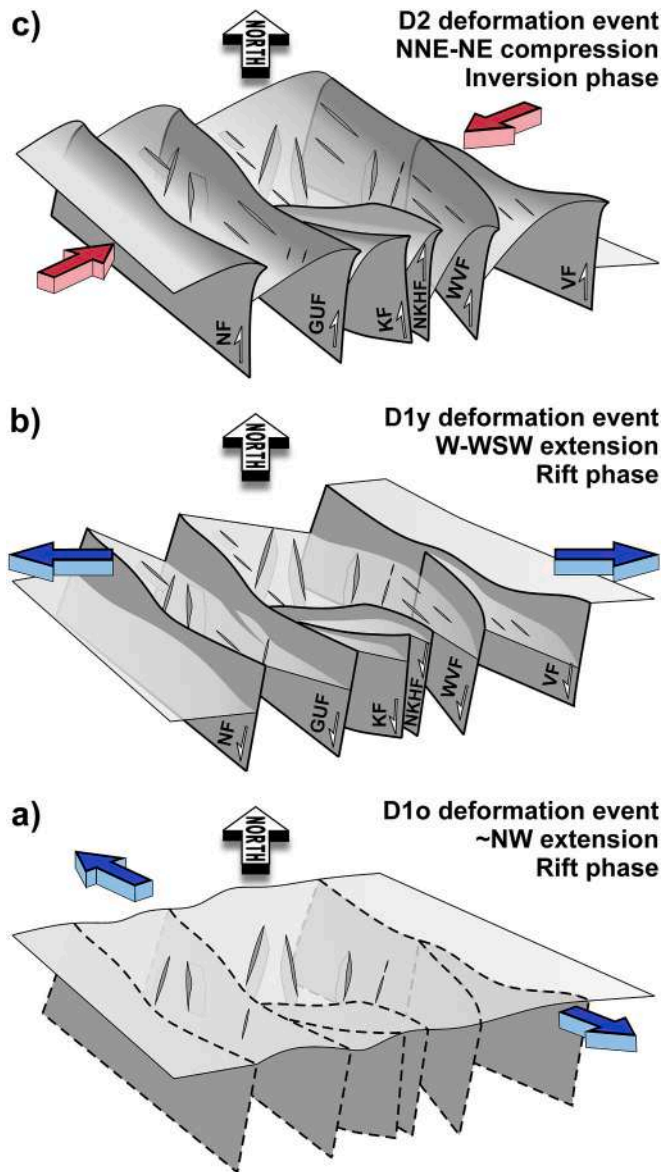
Fig. 16. Conceptual kinematic models to explain the effect of changing stress fields in the Vigodi-Gugriana-Khirasra-Netra Fault System (VGKNFS). Red, inward-pointed and blue, outward-pointed double arrows indicate the orientation of S_{Hmax} and S_{hmin} respectively. (a) D1o deformation event – Initiation of the rift phase of the KRB during Late Triassic. ~NW directed extension prevailed in the VGKNFS. Activation of NNE–NE striking discontinuous cross-faults as normal faults occurred. The NW striking pre-existing weak planes remained non-responsive. (b) D1y deformation event – continued rift phase of the KRB till Late Cretaceous. The extension direction swung from ~NW to W-WSW. Normal slip along the major NNW–NW striking faults occurred which eventually truncated the earlier activated NNE–NE striking cross-faults. (c) D2 deformation event – post-rift inversion phase of the KRB from Late Cretaceous till now. The build-up of NNE–NE directed compressional stress field that continues till now. The compressional reactivation of NNW–NW striking major faults occurred. NNE–NE striking cross-faults with normal slip continue to exist but remained non-responsive. The convex upward plunge of major faults in Fig. (c) indicate their upthrust geometry. Curved topography near major faults indicate narrow deformation zone. Note that the outcrop-scale structural complexities are ignored.

northernmost extremity, GUF at site 33 (sector 1) exposes striations with rake ranging 100–120° (measured with respect to N140° fault strike, Fig. 4d and e), while at its southernmost extremity, at site 41 (sector 4), GUF shows striations with rake 80–90° (measured with respect to N160°

fault strike, Fig. 13). Putting it all together, it can be inferred that the GUF acted as a rotational fault (/scissor fault/hinge fault) with no translational component involved with the axis of rotation lying perpendicular to the fault plane (e.g., Xu et al., 2011; models in Mukherjee and Tayade, 2019). The hangingwall on SW side of the GUF rotated anti-clockwise with respect to the fixed footwall lying on NE side. The anti-clockwise rotation of hangingwall involves downward movement at the northern extremity of GUF and upward movement at its southern extremity. The slip pattern observed along the GUF does not resemble the converging slip pattern along the normal faults described by Maniatis and Hampel (2008). The rotational fault (GUF) can be comparable with: the Alasehir basin in western Turkey (Oner and Dilek, 2013), Alhama de Murcia fault in eastern Betic Cordillera in southern Spain (Martınez-Dıaz, 2002).

The NW striking NKHF (site 99) and NE striking KF (sites 42, 57) with reverse slip, which are the bifurcations of NNW striking GUF, are exposed in sector 4 (Fig. 12). The NW striking NF exposed in sector 4 (sites 68, 89) shows reverse slip (Figs. 12 and S13). The unnamed, cross-faults are exposed in each sector. The NNE and NE striking faults show normal slip (e.g., site 71: Fig. 5) while the NW and E striking faults show reverse and/or normal slip.

The slickenside lineations are essentially straight, although Ghosh (1993) stated that purely translational faults seldom occur in nature. Curved stretching lineations are not observed on any of the fault planes. The synthetic shear has been observed in the exposed footwall/hangingwall in the sense that the development of secondary, synthetic, striated fault planes in the footwall indicate a domino-style deformation of the blocks and along with the principal slip surface, they have experienced downslope movement (e.g., Fig. 7). The carrot-shaped gouging-grain grooves developed *(i)* on the footwall of VF at site 27 (sector 3; Fig. 10c and d), their acute angle or concavity closes-up indicate the upward motion of missing hangingwall. *(ii)* Contrarily, at site 41 (sector 4) of the GUF, the carrot-shaped grooves are developed on the hangingwall with their acute angle closes-down indicate the downward motion of missing footwall (Fig. 13c, g). All the studied sites are characterized by a population of homogeneous fault-slip data and therefore, no superposition/cross-cutting/truncation of multiple generations of striations is observed except a single outcrop (in sector 3, Fig. 10h). The NNW striking unnamed fault exposes dip-slip striations (rake ~70°) that truncate almost horizontal striations (rake ~11°). This indicates that reverse dip-slip post-dates the sinistral strike-slip motion.

Simón (2019) pointed out divergence in paleostress analysis results when different methods are applied. To avoid such a situation and to better constrain the paleostress analysis results, we attempted different methods and cross-checked the results across four different programmes. We tested the same fault-slip data with *(i)* different paleostress analysis procedures (e.g., FaultKin and SG2PS) and, *(ii)* with same procedures (e.g., RDM applied in Win_Tensor and T-Tecto). The paleostress tensors obtained through Win_Tensor and FaultKin are in good agreement with each other in terms of the trend of three principal stress axes (Table 2). The parameter D of T-Tecto is similar to stress ratio (R) defined by Delvaux et al. (1997) and suggest the stress regime for each site in proximity to each other. The derived paleostress tensors show steep plunge of one principal stress axis and sub-horizontal to horizontal orientation of the other two. These indicate that the faults are non-Andersonian that have experienced changing stress fields temporally (Anderson, 1905; Yin and Ranalli, 1992). Since faults-slip data were collected on the ground surface, stress variation with depth is beyond the scope of the present work.

The GPR studies reveal reverse slip at site 36 (Fig. 14e–h) and normal slip at site 30 along the VF (Fig. S6); and reverse slip of the WVF along with the presence of cluster of deformation bands at site 34 (Fig. 14a–d). Thus, the fault geometry derived through GPR studies matches well with the surficial fault exposures. The slip-sense inferred through GPR studies is in agreement with the same derived by observing slickenside kinematic indicators on the exposed fault plane and it further improved our

degree of confidence.

The faults in the VGKNFS mark low cohesion. Therefore, they react to changing stress fields and record multiple movements. The segments of major faults with reverse slip are oriented perpendicular to the present-day compression. Therefore, they act as "weak" areas and may reactivate in the compressive stress regime. Another factor that may influence the reactivation is frictional weakening of faults (Shaw, 1995; review in Dutta and Mukherjee, 2019). Moreover, fault reactivation under ongoing compression is highly selective in the VGKNFS. In earlier studies (Sibson, 1995), it is inferred that only a few set of pre-existing normal faults or only individual segments of a normal fault strand reactivate during inversion and form reverse faults. The same tectonic scheme of preferential reactivation is observed in the VGKNFS, where NW striking major faults are reactivated under NNE striking present-day compression, while NNE, NE and E striking unnamed faults are unfavorably oriented and remain passive to the inversion phase. The disorientation of unnamed, cross-faults in the sense that their NNE, NE and E strike is having non-perpendicular relationship with the present-day S_{Hmax} orientation. Furthermore, the entire length of major NW striking faults in the VGKNFS did not reactivate. This is in spite of the fact that they are oriented favorably to the current NNE oriented S_{Hmax}. Owing to selective reactivation, the individual segments of fault strand reactivated during inversion. Two cases are – (i) only ~5 km lateral stretch (in sector 2) in the middle segment of the VF remained non-responsive to inversion, and (ii) the GUF that acts as a scissor fault. Its NW extremity (in sector 1) remained silent/inactive during inversion and persisted normal slip, while the rest other parts have witnessed reverse slip (in sectors 2, 3, 4).

The similar paleostress fields are grouped together and two major, distinct deformation events – older D1 and younger D2 are defined that correspond to the regional tectonic events. The older D1 deformation event is further divided into two sub-groups – older D1o and younger D1y. Each sub-group should be considered as sub-type of the major deformation event owing to their similarity with the far-field stress conditions. The deformation phases defined here are multi-phase as the orientation of principal stress axes remains constant during the individual sub-type of major deformation events (as in Fossen et al., 2019). Furthermore, they cannot be considered as progressive, since they are neither immediately preceding/following deformation phases nor showing gradual changes in stress orientations that may give rise to progressive deformation (Fossen et al., 2019). The deformation events are derived from the consistency among the deduced paleostress tensors from multiple paleostress analysis programmes. The age of faulted formations, attitude of principal stress axes, orientation of S_{Hmax} and S_{hmin}, stress regime index (R′) and the governing stress regime are the parameters used to interpret the paleostress tensors belonging to the same deformation event. The paleostress map shown in Fig. 15 represents the orientation of S_{Hmax} and S_{hmin} for reverse faults and normal faults, respectively, derived for each of the studied sites. Since no absolute age information of timing of faulting are available, the reconstruction of sequence of deformation events is mainly based on the relative age information deduced in the field. In the VGKNFS, the major faults viz., NW striking VF and GUF are older and dislocate/terminate other NNE, NE, E oriented unnamed faults.

6.1. Derivation of relative timing of paleostress state

6.1.1. Older D1 deformation event, Late Triassic to Late Cretaceous ~NW directed extension

The D1 event is characterized by paleostress tensors belonging to the extensional kinematics and is preferentially dominated by ~NW directed extension. W, NW, NNW and NE striking S_{hmin} are observed in each sector. They belong to the NW striking major faults as well as NE oriented unnamed normal faults of local occurrence that terminate against the major faults. D1 event is most favorably represented by NE striking unnamed normal faults. They could not reactivate in later times

due to their disorientation which is parallel to the ongoing compressional stress direction.

Following the data with normal fault kinematics in Sector 1, which mainly comprise of (i) NW directed extension represented by NE striking normal faults belonging to older D1o event (Fig. 16a), and (ii) WSW directed extension expressed by NNW striking GUF belonging to D1y event (Fig. 16b). These faults are formed under pure extensional stress regime with R′ ranging 0.31–0.61 (Fig. 15). Around 63% of paleostress tensors represent normal faults kinematics in sector 1.

52% of the paleostress tensors represent extensional stress field in sector 2. Two distinct trends of S_{hmin} are observed: (i) NNW–NW oriented extension expressed by ENE and NE striking unnamed subsidiary faults respectively belonging to D1o event (Fig. 16a), and (ii) ~W extension represented by NNW striking VF belonging to D1y event (Fig. 16b). Sector 2 constrains the VF showing normal and reverse slip-senses along its northern and southern segments, respectively. The northern segment is influenced by pure extensive to transtensive stress regime during D1y event and is characterized by ~W extension with R′ ranging from 0.38 to 0.50 (Fig. 15). In the vicinity of the northern segment of VF, N–NNE striking, sub-vertical, systematic joints (site 100) exposed in Jhuran sandstone are characterized by ~W extension with R′ of 0.99. The S_{hmin} strikes parallel to that of NNW striking VF with normal slip, testifying the fact that joints are generated during D1y event under transtensive stress regime. Thus, the systematic joints are related to far-field stresses and are not affected by local stress perturbations. Sector 2 also exposes WNW and ENE striking unnamed, subsidiary faults with normal slip belonging to pure extensive stress regime of D1o event. They are characterized by NNW oriented S_{hmin} with R′ of 0.49–0.64 (Fig. 15).

Sector 3 is characterized by (i) NE striking faults, (ii) E striking deformation band faults, (iii) NNE striking slipped deformation band, and (iv) NNW striking WVF. 45% of paleostress tensors represent extensional stress field in sector 3. NE striking subsidiary, unnamed faults show normal slip and are characterized by NW oriented S_{hmin} belonging to D1o event and are developed under pure extensive stress regime with R′ ranging from 0.49 to 0.67 (Fig. 16a). Nearly E striking deformation band fault formed under pure extensive to transtensive stress regime is represented by ~N striking S_{hmin} with R′ varying from 0.50 to 1.19. NNW striking WVF shows normal slip formed under pure extensive stress regime and is characterized by ~W striking S_{hmin} belonging to the D1y event with R′ ranging from 0.48 to 0.63 (Fig. 16b). Thus, temporally, NW to W rotation of S_{hmin} came about in sector 3.

In sector 4, NW striking normal fault of local occurrence is represented by NE striking S_{hmin}, which we argue that it has no role in the regional stress field. Except this one site, no other site in sector 4 shows signatures of extensional tectonics.

6.1.2. Younger D2 deformation event, Late Cretaceous to Quaternary fault reactivation under NNE–NE compression

We argue that the younger D2 event characterized by the compressive stress regime is the predominant structural style in the VGKNFS since Late Cretaceous. It is represented by NNE–NE compression and is the most dominant and best-fitted stress regime to the present-day stress conditions in each of the sector of VGKNFS. The paleostress regimes in the study area involve three major compression directions – NNE, NE and E.

Reverse fault kinematics during D2 event is expressed by NW striking VF and NNE striking unnamed faults in sector 1. Around 37% of paleostress tensors belong to D2 event in sector 1. In its northernmost extremity, the VF reactivated under transpressive stress regime with N24° directed S_{Hmax} and R′ of 2.03 belongs to the D2 event (Figs. 15 and 16c). Another set of NE striking reverse faults reactivated under transpressive to pure compressive stress regime and show N74°–N124° oriented S_{Hmax} with R′ of 2.19 and 2.53 (Fig. 15). We do not associate the ENE–ESE directed S_{Hmax} with the D2 event and propose that it is due to the local perturbations in the stress field.
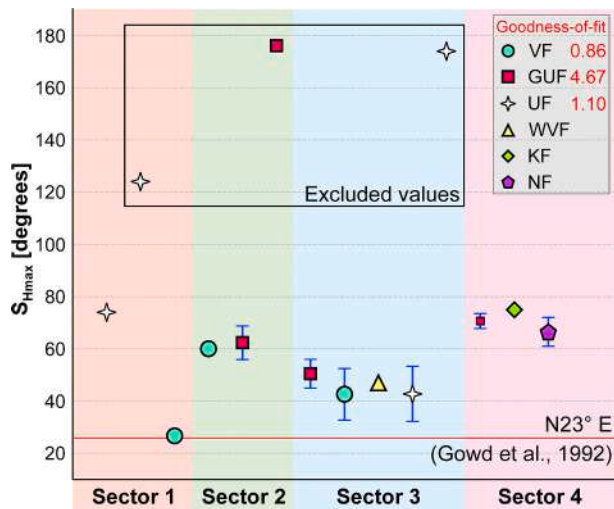
Fig. 17. Plot showing sector-wise distribution of the mean S_{Hmax} orientation corresponding to major faults and unnamed cross-faults with reverse slip. The results of chi-square statistic are also shown.

In sector 2, *(i)* the southern segment of VF and *(ii)* NW striking GUF with reverse slip are dominated by ~NE directed compression with R' ranging from 2.24 to 2.55 indicating the role of pure compressive stress regime (Fig. 16c). No unnamed cross-fault with NNE–E strike reactivated as reverse fault in sector 2. 48% of paleostress tensors represent compressional stress field in sector 2.

Sector 3 exposes NW striking VF and GUF, and NNW striking WVF that reactivated during D2 event under pure compressive stress regime with NNE–NE directed S_{Hmax} (Fig. 16c). Sector 4 exposes NNW striking GUF, and NW striking KF and NF that formed under pure compressive to transpressive stress regime with NE oriented S_{Hmax} (Fig. 16c). 55% and 88% of paleostress tensors represent D2 event in sectors 3 and 4 respectively.

6.2. Implications for tectonic evolution of western continental margin of the Indian plate

6.2.1. Relationship with the extensional rifting event

This corresponds to the rifting of the KRB and can be correlated with the tectonic cycle 1 of extensional rift stage described by Biswas (2016). The cycle 1 emphasizes tensional activation of major faults in the KRB. The KRB is a failed rift (Biswas, 1982). The younger D1y and older D1o events with W–WSW and NW oriented S_{hmin}, respectively, belong to the extensional rifting event (Fig. 16a and b). The KRB rifted in the Late Triassic or Early Jurassic prior to India-Africa separation (Biswas, 2016). This is related to early stage of break-up of the Gondwanaland. The rifting then aborted during Late Cretaceous (Biswas, 2016). The rifting caused the build-up of extensional stresses in the KRB. The extensional stresses activated the E-W striking major faults and other subsidiary faults. These faults activated along the NE trend of Mid-Proterozoic Aravalli-Delhi fold belt which swings to E-W in the KRB (Biswas, 1987, 2016). This led to the growth of variably oriented normal faults. In a similar context, regions other than the KRB also experienced extensional stresses. For example, Tiwari et al. (2020) reported extensional tectonics with NW-SE oriented extension from Ambaji (~400 km east of VGKNFS) in the Aravalli-Delhi mobile belt and linked it with the Gondwanaland assembly.

Also, in the Middle Jurassic to Early Cretaceous, continental fragmentation of eastern Gondwana led to the separation of India from Australia and Antarctica (Gibbons et al., 2013). The rotational rifting with earlier orthogonal rifting and subsequent highly oblique rifting (>45°) between India and Australia occurred (Brune et al., 2018; Zwaan and Schreurs, 2020). This led to the generation of ~W directed slip

vectors at 130 Ma and ~NW directed slip vectors at 120 Ma at the western continental margin of the Indian plate (Brune et al., 2018). This may have influenced the extensional stress field in the KRB during Early Cretaceous.

6.2.2. Relationship with the anticlockwise rotation of the Indian plate during Cretaceous

After the break-up of the Gondwanaland and India-Africa separation, drift movement of the Indian plate began with counter-clockwise rotation from Mid-Jurassic time onward (Chatterjee et al., 2013). This induced transtensional movement in the KRB (Biswas, 2016). Although, strike-slip motion is not prominent and no structural signatures of transtensional stress regime are observed on regional scale in the VGKNFS. None of the major faults in the VGKNFS display strike-slip motion. Sites with transpressional (e.g., site 6: GUF)/transtensional (e. g., site 23: VF) tectonics are due to local perturbations in the stress field and these do not mean that the VGKNFS experienced an overall transpressional/transtensional stress regimes. The striated faults denoting strike-slip motion are of sporadic occurrence (e.g., Fig. 10e: site 27 and Fig. 10h: ~3.5 km NE of site 87). The dip-slip striations clearly seem to truncate strike-slip striations indicating that reverse movement is younger than strike-slip motion in the VGKNFS. On a regional context, the above observations match well in the sense that the inversion of the KRB post-dates the drift of the Indian plate. Due to lack of sufficient number of fault-slip data with strike-slip motion (nt = 2), it is not included in the paleostress analysis. Therefore, we did not assign separate deformation event to strike-slip motion as the paleostress orientations are unknown.

6.2.3. Fault reactivation during basin inversion and its relation to Cenozoic Indian-Eurasian plate collision kinematics

The D2 event with NNE–NE oriented S_{Hmax} belonging to compressional stress regime (Late Cretaceous – till now) is expressed by NW striking major faults in the VGKNFS (Fig. 16c). The rifting of the KRB is followed by the rift inversion phase (tectonic cycle 2; as in Biswas, 2016). The NW striking major faults in the VGKNFS dip at high-angle but not sub-vertical. So, there is no question that they will get locked in inversion tectonics. As the far-field compressive stresses are at right angles, the normal faults formed during rifting, reactivated as high-angle reverse faults and certainly, there is not any possibility that they resolved into strike-slip motion. Therefore, the VGKNFS cannot be interpreted as the riedel shear system bounded by the KMF and KHF.

The compressional stress field with NNE–NE oriented S_{Hmax} is generated by: *(i)* collision of the Indian plate with the southern margin of Eurasia at the convergent margin in Late Paleocene–Eocene. This generated N–NE verging back-thrust at the collision front (Gowd et al., 1992). This vergence of backthrusting happened in the Himalaya and it is now well-documented and discussed (Bose and Mukherjee, 2019a, b). The post-Indian-Eurasian plate collisional far-field compressive stress field is continuing till date causing neotectonic movements in the KRB (Biswas, 2016; Shaikh et al., 2019b). *(ii)* The spreading Carlsberg ridge at the divergent margin in the Indian Ocean exerts horizontal ridge push force resulting from the excess thermal elevation of young oceanic lithosphere (Eagles and Wibisono, 2013). It generated intra-plate stresses ENE towards the KRB and contributed to the Indian plate motion (Biswas, 2016). Along the western Indian plate margin, the Chaman fault system with left-lateral strike-slip motion does not contribute to build-up of intra-plate stresses in the KRB.

6.3. Congruence with the present-day stress state

It would be interesting to compare the paleostress field inferred from the present work with the contemporary stress field in the KRB. Till date, no studies have been carried out to infer present-day stress state in the study area. However, myriad work has been done in the eastern part of the KRB that can be accounted for comparison with paleostress

conditions inferred in the study area at the western part of the KRB. Several studies related to inversion of earthquake FMS (Mandal, 2013 and references therein), GPS derived surface displacement measurements (Dumka et al., 2019; Gahalaut et al., 2019 and references therein), InSAR data (Chandrasekhar et al., 2009 and references therein) and offshore BO (Sen et al., 2019 and references therein) provide extensive constraints on the recent kinematics of the active KRB. For example, Richardson et al. (1979) computed ~N oriented S_{Hmax}. Gowd et al., 1992 estimated mean S_{Hmax} to be N23° E for the mid-continental stress province of India (central and northern India) using BO (~1–3.5 km depth), FMS (~15–33 km depth) and hydrofracturing (~150–590 m depth) data. The World Stress Map (WSM) compiled compressional faulting regime with N02°–05° E and N148°–178° E striking S_{Hmax}, and strike-slip faulting regime with N152°–178° E and N14° E striking S_{Hmax} using FMS; and NE oriented S_{Hmax} using BO in the eastern part of the KRB, ~120–150 km east of the present study area (Heidbach et al., 2016, 2018). Sen et al. (2019) interpreted S_{Hmax} to be N10°–N20° E using BO in the offshore Kachchh-Saurashtra region. Mallik et al. (2008) carried out Electromagnetic Radiation (EMR) investigations to infer the S_{Hmax} to be N60° E ± 10°. Patra and Saha (2019) also reported N-S compression from eastern Himalaya. Our paleostress analysis results belonging to D2 event are consistent with the inferred present-day kinematics in the sense that the NW striking major, reactivated reverse faults in the VGKNFS show NNE–NE striking S_{Hmax} (see Section 6.1.2). Follow Table S2 (Supplementary data) for the list of selected references discussing about the present-day kinematics prevailing in the KRB.

6.4. Is the VGKNFS really sensitive to the far-field stress?

6.4.1. Chi-square statistic

We adopted a statistical approach to address the question mentioned above. The goodness-of-fit test was performed to analyze the chi-square statistic. Goodness-of-fit calculation is a statistical hypothesis that provides a way to assess how well the obtained S_{Hmax} orientations through paleostress analysis fit with the ongoing NNE directed compressional stress field. Mean S_{Hmax} orientation derived for major and unnamed cross-faults through paleostress analysis was taken as the input parameter. The limitations of this analysis are:

(i) faults with reverse slip are included in the analysis while the major and unnamed faults with normal slip are excluded,

(ii) the test requires a sufficient sample size of S_{Hmax} orientation to establish chi-square approximation to be valid and therefore, goodness-of-fit calculation could not be performed for the WVF (number of observations $i = 2$), KF ($i = 2$), NF ($i = 2$) and slipped deformation band ($i = 1$).

The results are represented in the form of a chart as shown in Fig. 17. The test was performed using the following equation:

$$\chi^2 = \frac{\left\{ (S_{Hmax})_{mean} - (S_{Hmax})_{predicted} \right\}^2}{\left\{ (S_{Hmax})_{std.\ dev.} \right\}^2} \quad \text{(eq. 1)}$$

Here, χ^2 = chi squared value calculated as the goodness-of-fit function, $(S_{Hmax})_{mean}$ = mean orientation of S_{Hmax} calculated through paleostress analysis in the present study, $(S_{Hmax})_{predicted}$ = NNE oriented S_{Hmax} in the contemporary compressional stress field, $(S_{Hmax})_{std.\ dev.}$ = standard deviation of a range of orientations of S_{Hmax} computed through paleostress analysis in the present study.

The mean S_{Hmax} orientation of VF, WVF, GUF, KF, NF and unnamed cross-faults were calculated for each of the sectors and plotted on the graph. The uncertainty or variability in the population of calculated S_{Hmax} orientations was estimated by calculating standard error for the respective fault in each of the four sectors. The calculated standard error has been graphically represented in the form of an error bar (Fig. 17). The red horizontal line depicts the mean S_{Hmax} of N23° E derived by

Gowd et al., 1992 using BO-, FSM- and hydrofracturing data. The mean S_{Hmax} orientations not falling in the N0°–90° E interval were excluded (indicated by black box area in Fig. 17).

In the scenario of VGKNFS, we might reasonably consider:

(i) $\chi^2 \leq 1$; represented by the observed values fall within the data uncertainty. The measured S_{Hmax} orientations to have a "good" fit to the regional contemporary NNE oriented compressional stress field. The VF ($\chi^2 = 0.86$) shows close fit with the ongoing NNE oriented compression stress field. It also points to the likelihood of fault reactivation, although, other important parameters e.g., the observed fault geometry combined with estimated stress orientation and magnitude should also be taken into account.

(ii) $\chi^2 > 1$; represented by any observed values that fall outside the data uncertainty interval. The calculated S_{Hmax} orientations to have a "poor" fit to the contemporary NNE oriented compressional stress field. The GUF ($\chi^2 = 4.67$) shows the highest discrepancy or skewness between the calculated S_{Hmax} and the ongoing NNE oriented S_{Hmax}. Since the goodness-of-fit value for unnamed cross-faults ($\chi^2 = 1.10$) is very close to 1, it can be considered that the derived S_{Hmax} orientations for the unnamed cross-faults with reverse slip fairly match with the contemporary NNE oriented compressional stress field.

6.4.2. Regions illustrating maximum horizontal compression in VGKNFS and their relevance to the Indian plate motion

The paleostress map depicted in Fig. 15 highlights the density of S_{Hmax} orientations. The potential zones of stress accumulation are highlighted by warm colors. The mean S_{Hmax} orientations in the compressional stress regime, obtained for the major faults in each of the sectors, can be correlated with the convergence(/absolute plate motion) direction of the Indian plate. The convergence direction is nearly orthogonal to NE boundary of the Indian plate (Lacombe, 2012). The absolute plate motion direction of the Indian plate is ~N40° E (Singh and Mandal, 2020). From sector 1 to 4, the angle of divergence are 16°, 22°, 06° and 30° respectively. Thus, statistically, it can be inferred that sector 3 showing highest uplift in the VGKNFS, exhibits less obliquity to the Indian plate convergence direction than those in the other sectors. In the intra-plate regions characterized by compressional stress regime, the orientation of S_{Hmax} is generally parallel to the direction of absolution plate motion (Zoback et al., 1989). Thus, in the present study, (i) low divergence-angle of S_{Hmax} to the Indian plate convergence direction and, (ii) spatial homogeneity of the *in situ* stress field, in both, reverse and normal faulting stress regime suggest that the far-field stresses dominate over the near-field stress condition to govern the intra-plate stress distribution in the VGKNFS.

7. Conclusions

The brittle structures were measured at 66 sites and 1150 fault-slip data were collected from the Vigodi-Gugriana-Khirasra-Netra Fault System (VGKNFS). It permitted us to reconstruct the regional paleostress field and to unfold the polyphase tectonic history. The relative age of faulting inferred through field observations and the knowledge of successive regional tectonic events provided constraints on timing of the derived paleostress fields.

1. Since the faults are exposed in uniform lithology, slip-sense is inferred by observing various slickenside kinematic indicators. Carrot-shaped and pipe-shaped gouging grain grooves, mineral steps, fractures with different morphologies, domino-type offsetting in footwall/hangingwall, drag folding etc. are found useful in deciphering normal/reverse slip-sense.

2. The paleostress tensors obtained through Win_Tensor, T-Tecto, FaultKin and SG2PS are in good agreement with each other. Although, some show discrepancy in terms of the orientation of three

principal stress axes. The results suggest that the VGKNFS encompasses non-Andersonian faulting with the temporally changing stress-fields. GPR surveys reveal – *(i)* normal slip at site 30 along the Vigodi Fault (VF) (sector 2), *(ii)* reverse slip at site 36 along the VF (sector 3) and, *(iii)* reverse slip of the West Vigodi Fault (WVF) along with the presence of deformation bands cluster at site 34 (sector 3). The fault geometry and slip-sense inferred through GPR profiles comply with our structural observations.

3. The statistical analysis using chi-square goodness-of-fit test was performed on the derived paleostress analysis results. The test implies the probability of fault reactivation in VGKNFS. The VF ($\chi^2 = 0.86$) and unnamed faults ($\chi^2 = 1.10$) with reverse slip show good fit while the Gugriana Fault (GUF) ($\chi^2 = 4.67$) shows poor fit with the contemporary compressional stress field with NE–NNE oriented S_{Hmax}.

4. Two major deformation events – older D1 and younger D2 are defined based on the paleostress analysis results. The D1 event is associated with extensional kinematics, governing from Late Triassic to Late Cretaceous. It is further divided into two sub-groups – older D1o and younger D1y. The D1y event shows W–WSW oriented S_{hmin} attributed to NNW–NW striking GUF and VF. The D1o event shows NNW–NW oriented S_{hmin}, near-perpendicular to the NE, ENE strike of unnamed cross-faults. The break-up of the Gondwanaland led to the rifting of KRB. This caused the build-up of extensional stresses in the KRB and formed normal faults during D1 event. After India-Africa separation, counter-clockwise drift of the Indian plate began from Mid-Jurassic time onward. This caused the strike-slip motion of earlier activated normal faults in the KRB. However, none of the major faults in the VGKNFS preserve any significant evidences of strike-slip motion.

5. The D2 event, governing from Late Cretaceous to the present times, is related to positive inversion of the KRB and is characterized by NNE–NE oriented S_{Hmax}. It is mainly expressed by compressional reactivation of NW–NNW striking VF, WVF, GUF, Khirasra Fault (KF), North Khirasra Fault (NKHF) and Netra Fault (NF). A large part of the compressive stresses are accommodated in the intra-uplift fault zones (e.g., in the VGKNFS) as evidenced by the reverse nature of major faults (e.g., VF and GUF), than the uplift-bounding faults (e.g., KMF). The far-field compressional stress field is generated by: *(i)* back-thrust from the Indian-Eurasian plate collision at the convergent margin during Late Paleocene–Eocene and, *(ii)* the spreading Carlsberg ridge at the divergent margin in the Indian Ocean that exerts horizontal ridge push force to the KRB.

6. Compressional reactivation of faults in the VGKNFS is highly selective. The entire length of NW striking VF did not reactivate, though, it is optimally oriented to the current NNE directed S_{Hmax}. The NW (in sector 1) and SE (in sectors 3, 4) segments of the VF show reverse slip. While, only ~5 km lateral stretch (in sector 2) in the middle segment show normal slip and thus, it remained silent during D2 event. The NW striking GUF acts as a scissor fault. At its NW extremity (in sector 1), the GUF remained non-responsive during D2 event while in rest other parts, the GUF has witnessed reverse slip (in sectors 2, 3, 4). NNE, NE striking unnamed cross-faults exposed in all the four sectors did not undergo compressional reactivation due to their unfavorable orientation. The nature of preferential reactivation of faults is due to the uneven distribution of compressive stresses during D2 event within the intra-uplift VGKNFS.

CRediT authorship contribution statement

Mohamedharoon A. Shaikh: Conceptualization, Methodology, Software, Formal analysis, Investigation, Writing - original draft, Writing - review & editing. **Deepak M. Maurya:** Conceptualization, Methodology, Validation, Investigation, Resources, Writing - review & editing, Supervision, Project administration, Funding acquisition. **Soumyajit Mukherjee:** Conceptualization, Methodology, Writing - review & editing, Supervision. **Naimisha P. Vanik:** Investigation. **Akash Padmalal:** Investigation. **Laxman S. Chamyal:** Supervision, Investigation, Project administration, Funding acquisition.

Declaration of competing interest

The authors declare that they have no known competing financial interests or personal relationships that could have appeared to influence the work reported in this paper.

Acknowledgements

Appendix A. Supplementary data

Supplementary data to this article can be found online at https://doi.org/10.1016/j.jsg.2020.104124.

References

Allmendinger, R.W., Cardozo, N.C., Fisher, D., 2012. Structural Geology Algorithms: Vectors & Tensors. Cambridge University Press, Cambridge.

Anderson, E.M., 1905. The dynamics of faulting. Trans. Edinb. Geol. Soc. 8 (3), 387–402. https://doi.org/10.1144/transed.8.3.387.

Angelier, J., 1990. Inversion of field data in fault tectonics to obtain the regional stress. A new rapid direct inversion method by analytical means. Geophys. J. Int. 103 (2), 363–376. https://doi.org/10.1111/j.1365-246X.1990.tb01777.x.

Angelier, J., 1994. Fault slip analysis and paleostress reconstruction. In: Hancock, P.L. (Ed.), Continental Deformation. Pergamon Press, Oxford, pp. 53–101.

Beauchamp, W., Barazangi, M., Demnati, A., Alji, M.E., 1996. Intracontinental rifting and inversion: Missour basin and Atlas mountains, Morocco. AAPG Bull. 80 (9), 1459–1481. https://doi.org/10.1306/64ED9A60-1724-11D7-8645000102C1865D.

Bendick, R., Bilham, R., Fielding, E., Gaur, V.K., Hough, S.E., Kier, G., Kulkarni, M.N., Martin, S., Mueller, K., Mukul, M., 2001. The 26 january 2001 "republic day" earthquake, India. Seismol Res. Lett. 72 (3), 328–335. https://doi.org/10.1785/gssrl.72.3.328.

Bhattacharya, F., Chauhan, G., Prasad, A.D., Patel, R.C., Thakkar, M.G., 2019. Strike-slip faults in an intraplate setting and their significance for landform evolution in the Kachchh peninsula, Western India. Geomorphology 328, 118–137. https://doi.org/10.1016/j.geomorph.2018.12.006.

Bilham, R., 1999. Slip parameters for the Rann of Kachchh, India, 16 June 1819, earthquake, quantified from contemporary accounts. Geological Society, London, Special Publications 146 (1), 295–319. https://doi.org/10.1144/GSL.SP.1999.146.01.18.

BIS, 2002. IS 1893–2002 (Part 1): Indian Standard Criteria for Earthquake Resistant Design of Structures, Part 1–General Provisions and Buildings. Bureau of Indian Standards, New Delhi. Retrieved from. https://bis.gov.in/other/quake.htm.

Biswas, S.K., 1982. Rift basins in western margin of India and their hydrocarbon prospects with special reference to Kutch basin. AAPG (Am. Assoc. Pet. Geol.) Bull. 66 (10), 1497–1513. https://doi.org/10.1306/03B5A976-16D1-11D7-8645000102C1865D.

Biswas, S.K., 1987. Regional tectonic framework, structure and evolution of the western marginal basins of India. Tectonophysics 135 (4), 307–327. https://doi.org/10.1016/0040-1951(87)90115-6.

Biswas, S.K., 1993. Geology of Kachchh. K. D. Malaviya Institute of Petroleum Exploration, Dehradun.

Biswas, S.K., 2005. A review of structure and tectonics of Kutch basin, western India, with special reference to earthquakes. Curr. Sci. 88 (10), 1592–1600.

Biswas, S.K., 2016. Tectonic Framework, Structure and Tectonic Evolution of Kutch Basin, Western India, vol. 6. Special publication of the geological society of India, pp. 129–150. https://doi.org/10.17491/cgsi%2F2016%2F105417. Retrieved from.

Biswas, S.K., Khattri, K.N., 2002. A geological study of earthquakes in Kutch, Gujarat, India. Geological Society of India 60 (2), 131–142.

Bose, N., Mukherjee, S., 2019a. Field documentation and genesis of the back-structures from the Garhwal Lesser Himalaya, Uttarakhand, India. Geological Society, London, Special Publications 481, 111–125. https://doi.org/10.1144/SP481-2018-81.

Bose, N., Mukherjee, S., 2019b. Field documentation and genesis of back-structures in ductile and brittle regimes from the foreland part of a collisional orogen: examples from the Darjeeling–Sikkim Lesser Himalaya, India. International Journal of Earth Sciences 108 (4), 1333–1350. https://doi.org/10.1007/s00531-019-01709-7.

Bott, M.H.P., 1959. The mechanics of oblique slip faulting. Geol. Mag. 96 (2), 109–117. https://doi.org/10.1017/S0016756800059987.

Brune, S., Williams, S.E., Muller, R.D., 2018. Oblique rifting: the rule, not the exception. Solid Earth 9, 1187–1206. https://doi.org/10.5194/se-9-1187-2018.

Butler, M., Pullan, C.P., 1990. Tertiary structures and hydrocarbon entrapment in the Weald Basin of southern England. Geological Society, London, Special Publications 55 (1), 371–391. https://doi.org/10.1144/GSL.SP.1990.055.01.19.

Chandra, U., 1977. Earthquakes of peninsular India- a seismotectonic study. Bull. Seismol. Soc. Am. 67 (5), 1387–1413. Retrieved from. https://pubs.geosciencewor ld.org/ssa/bssa/article-abstract/67/5/1387/117753/earthquakes-of-peninsular-in dia-a-seismotectonic?redirectedFrom=PDF.

Chandrasekhar, D.V., Bürgmann, R., Reddy, C.D., Sunil, P.S., Schmidt, D.A., 2009. Weak mantle in NW India probed by geodetic measurements following the 2001 Bhuj earthquake. Earth Planet Sci. Lett. 280 (1-4), 229–235. https://doi.org/10.1016/j. epsl.2009.01.039.

Chatterjee, S., Goswami, A., Scotese, C.R., 2013. The longest voyage: tectonic, magmatic, and paleoclimatic evolution of the Indian plate during its northward flight from Gondwana to Asia. Gondwana Res. 23 (1), 238–267. https://doi.org/10.1016/j. gr.2012.07.001.

Choudhury, P., Chopra, S., Kumar, M.R., 2018. A review of seismic hazard assessment of Gujarat: a highly active intra-plate region. Earth Sci. Rev. 187, 205–218. https://doi. org/10.1016/j.earscirev.2018.09.014.

Chowksey, V., Joshi, P., Maurya, D.M., Chamyal, L.S., 2011a. Ground penetrating radar characterization of fault-generated Quaternary colluvio-fluvial deposits along the seismically active Kachchh Mainland Fault, Western India. Curr. Sci. 100 (6), 915–921. Retrieved from. http://www.jstor.org/stable/24076485.

Chowksey, V., Maurya, D.M., Joshi, P., Khonde, N., Das, A., Chamyal, L.S., 2011b. Lithostratigraphic development and neotectonic significance of the Quaternary sediments along the Kachchh Mainland Fault (KMF) zone, western India. Journal of Earth System Science 120 (6), 979–999. https://doi.org/10.1007/s12040-011-0123-0.

Chung, W.Y., Gao, H., 1995. Source parameters of the Anjar earthquake of July 21, 1956, India, and its seismotectonic implications for the Kutch rift basin. Tectonophysics 242 (3-4), 281–292. https://doi.org/10.1016/0040-1951(94)00203-L.

Dasgupta, S., Pande, P., Ganguly, D., Iqbal, Z., Sanyal, N.V., et al., 2000. Seismotectonic Atlas of India and its Environs. Geological Survey of India.

Davies, R., Cloke, I., Cartwright, J., Robinson, A., Ferrero, C., 2004. Post-breakup compression of a passive margin and its impact on hydrocarbon prospectivity: an example from the Tertiary of the Faeroe–Shetland Basin, United Kingdom. AAPG Bull. 88 (1), 1–20. https://doi.org/10.1306/09030303008.

Delvaux, D., Sperner, B., 2003. New aspects of tectonic stress inversion with reference to the TENSOR program. Geological Society, London, Special Publications 212, 75–100. https://doi.org/10.1144/GSL.SP.2003.212.01.06.

Delvaux, D., Moeys, R., Stapel, G., Petit, C., Levi, K., Miroshnichenko, A., Ruzhich, V., San'kov, V., 1997. Paleostress reconstructions and geodynamics of the Baikal region, Central Asia, Part 2. Cenozoic rifting. Tectonophysics 282 (1-4), 1–38. https://doi. org/10.1016/S0040-1951(97)00210-2.

Doblas, M., 1998. Slickenside kinematic indicators. Tectonophysics 295 (1-2), 187–197. https://doi.org/10.1016/S0040-1951(98)00120-6.

Doblas, M., Mahecha, V., Hoyos, M., Loīpez-ruiz, J., 1997. Slickenside and fault surface kinematic indicators on active normal faults of the Alpine Betic cordilleras, Granada, southern Spain. J. Struct. Geol. 19 (2), 159–170. https://doi.org/10.1016/S0191-8141(96)00086-7.

Dumka, R.K., Chopra, S., Prajapati, S., 2019. GPS derived crustal deformation analysis of Kachchh, zone of 2001 (M7.7) earthquake, Western India. Quat. Int. 507, 295–301. https://doi.org/10.1016/j.quaint.2019.01.032.

Dutta, D., Mukherjee, S., 2019. Opposite shear senses: geneses, global occurrences, numerical simulations and a case study from the Indian western Himalaya. J. Struct. Geol. 126, 357–392. https://doi.org/10.1016/j.jsg.2019.05.008.

Eagles, G., Wibisono, A.D., 2013. Ridge push, mantle plumes and the speed of the Indian plate. Geophys. J. Int. 194 (2), 670–677. https://doi.org/10.1093/gji/ggt162.

Etchecopar, A., Vasseur, G., Daignieres, M., 1981. An inverse problem in microtectonics for the determination of stress tensors from fault striation analysis. J. Struct. Geol. 3 (1), 51–65. https://doi.org/10.1016/0191-8141(81)90056-0.

Federico, L., Crispini, L., Vigo, A., Capponi, G., 2014. Unravelling polyphase brittle tectonics through multi-software fault-slip analysis: the case of the Voltri Unit, Western Alps (Italy). J. Struct. Geol. 68 (part A), 175–193. https://doi.org/10.1016/ j.jsg.2014.09.011.

Fossen, H., Cavalcante, G.C.G., Pinheiro, R.V.L., Archanjo, C.J., 2019. Deformation–progressive or multiphase? J. Struct. Geol. 125, 82–99. https://doi. org/10.1016/j.jsg.2018.05.006.

Gahalaut, V.K., Gahalaut, K., Dumka, R., Chaudhury, P., Yadav, R.K., 2019. Geodetic evidence of high compression across seismically active Kachchh paleo-rift, India. Tectonics 38, 3097–3107. https://doi.org/10.1029/2019TC005496.

Geophysical Survey Systems, 2012. Technical Manual: Radan V. 7. Geophysical survey systems (GSSI), Inc., Salem, New Hampshire, Unites states.

Ghosh, S.K., 1993. Structural Geology: Fundamentals and Modern Developments. Pergamon Press, p. 429.

Giambiagi, L., Alvarez, P., Spagnotto, S., 2016. Temporal variation of the stress field during the construction of the central Andes: constrains from the volcanic arc region (22–26°S), Western Cordillera, Chile, during the last 20 Ma. Tectonics 35 (9), 2014–2033. https://doi.org/10.1002/2016TC004201.

Giambiagi, L., Alvarez, P., Creixell, C., Mardonez, D., Murillo, I., Velasquez, R., Lossada, A., Suriano, J., Mescua, J., Barrionuevo, M., 2017. Cenozoic shift from compression to strike-slip stress regime in the High Andes at 30° S, during the shallowing of the slab: implications for the El Indio/Tambo mineral district. Tectonics 36 (11), 2714–2735. https://doi.org/10.1002/2017TC004608.

Gibbons, A.D., Whittaker, J.M., Müller, R.D., 2013. The breakup of East Gondwana: assimilating constraints from Cretaceous ocean basins around India into a best-fit tectonic model. J. Geophys. Res.: solid earth 118 (3), 808–822. https://doi.org/ 10.1002/jgrb.50079.

Gowd, T.N., Rao, S.S., Gaur, V.K., 1992. Tectonic stress field in the Indian subcontinent. J. Geophys. Res.: Solid Earth 97 (B8), 11879–11888. https://doi.org/10.1029/ 91JB03177.

Heidbach, O., Rajabi, M., Cui, X., Fuchs, K., Müller, B., Reinecker, J., Reiter, K., Tingay, M., Wenzel, F., Xie, F., Ziegler, M.O., Zoback, M.L., Zoback, M., 2018. The World Stress Map database release 2016: crustal stress pattern across scales. Tectonophysics 744, 484–498. https://doi.org/10.1016/j.tecto.2018.07.007.

Heidbach, O., Rajabi, M., Reiter, K., Ziegler, M., 2016. World Stress Map 2016, GFZ Data Service. https://doi.org/10.5880/WSM.2016.002.

Kaven, J.O., Maerten, F., Pollard, D.D., 2011. Mechanical analyses of fault slip data: implications for paleostress analyses. J. Struct. Geol. 33 (2), 78–91. https://doi.org/ 10.1016/j.jsg.2010.12.004.

King, P.R., Thrasher, G.P., 1992. Post-Eocene development of the Taranaki Basin, New Zealand: convergent overprint of a passive margin. In: Watkins, J.S., Zhiqiang, F., McMillan, K.J. (Eds.), Geology and Geophysics of Continental Margins, vol. 53. American Association of Petroleum Geologists Memoir, pp. 93–118. https://doi.org/ 10.1306/M53552C7.

Kothyari, G.C., Dumka, R.K., Singh, A.P., Chauhan, G., Thakkar, M.G., Biswas, S.K., 2016. Tectonic evolution and stress pattern of south Wagad Fault at the Kachchh rift basin in western India. Geol. Mag. 154 (4), 875–887. https://doi.org/10.1017/ S0016756816000509.

Lacombe, O., 2012. Do fault slip data inversions actually yield "paleostresses" that can be compared with contemporary stresses? A critical discussion. Compt. Rendus Geosci. 344 (3-4), 159–173. https://doi.org/10.1016/j.crte.2012.01.006.

Lewis, C.J., Baldridge, W.S., 1994. Crustal extension in the Rio Grande rift, New Mexico: half-grabens, accommodation zones, and shoulder uplifts in the Ladron Peak-Sierra Lucero area. In: Keller, G.R., Cather, S.M. (Eds.), Basins of the Rio Grande Rift: Structure, Stratigraphy, and Tectonic Setting, vol. 291, pp. 135–156. https://doi. org/10.1130/SPE291-p135.

Maestro, A., Ruano, P., Carbonell, P.T., Bohoyo, F., Galindo-Zaldívar, J., Pedrera, A., Ruiz-Constán, A., González-Castillo, L., Ibarra, P., López-Martínez, J., 2018. Stress field evolution of the southernmost Andean Cordillera from paleostress analysis (Argentine Tierra del Fuego). Tectonics 38 (1), 7–25. https://doi.org/10.1029/ 2018TC005158.

Mallik, J., Mathew, G., Angerer, T., Greiling, R.O., 2008. Determination of directions of horizontal principal stress and identification of active faults in Kachchh (India) by electromagnetic radiation (EMR). J. Geodyn. 45 (4-5), 234–245. https://doi.org/ 10.1016/j.jog.2008.01.003.

Mandal, P., 2013. Seismogenesis of the uninterrupted occurrence of the aftershock activity in the 2001 Bhuj earthquake zone, Gujarat, India, during 2001–2010. Nat. Hazards 65 (2), 1063–1083. https://doi.org/10.1007/s11069-012-0115-7.

Maniatis, G., Hampel, A., 2008. Along-strike variations of the slip direction on normal faults: insights from three-dimensional finite-element models. J. Struct. Geol. 30 (1), 21–28. https://doi.org/10.1016/j.jsg.2007.10.002.

Marrett, R.A., Allmendinger, R.W., 1990. Kinematic analysis of fault-slip data. J. Struct. Geol. 12 (8), 973–986. https://doi.org/10.1016/0191-8141(90)90093-E.

Martınez-Dıaz, J.J., 2002. Stress field variation related to fault interaction in a reverse oblique-slip fault: the Alhama de Murcia fault, Betic Cordillera, Spain. Tectonophysics 356 (4), 291–305. https://doi.org/10.1016/S0040-1951(02)00400-6.

Martino, R.D., Guereschi, A.B., Montero, A.C., 2016. Reactivation, inversion and basement faulting and thrusting in the Sierras Pampeanas of Córdoba (Argentina) during Andean flat-slab deformation. Geol. Mag. 153 (5-6), 962–991. https://doi. org/10.1017/S0016756816000339.

Maurya, D.M., Chowksey, V., Joshi, P.N., Chamyal, L.S., 2013. Application of GPR for delineating the neotectonic setting and shallow subsurface nature of the seismically active Gedi fault, Kachchh, western India. J. Geophys. Eng. 10 (3), 034006 https:// doi.org/10.1088/1742-2132/10/3/034006.

Maurya, D.M., Chowksey, V., Patidar, A.K., Chamyal, L.S., 2016. A Review and New Data on Neotectonic Evolution of Active Faults in the Kachchh Basin, Western India: Legacy of Post-deccan Trap Tectonic Inversion, vol. 445. Geological Society of London Special Publication, pp. 237–268. https://doi.org/10.1144/SP445.7.

Maurya, D.M., Chowksey, V., Tiwari, P., Chamyal, L.S., 2017. Tectonic geomorphology and neotectonic setting of the seismically active South Wagad Fault (SWF), Western India, using field and GPR data. Acta Geophys. 65 (6), 1167–1184. https://doi.org/10.1007/s11600-017-0099-5.

Maurya, D.M., Thakkar, M.G., Chamyal, L.S., 2003. Implications of transverse fault system on tectonic evolution of Mainland Kachchh, western India. Curr. Sci. 85 (5), 661–666. Retrieved from. http://www.jstor.org/stable/24109108.

Miller, J.F., Mitra, S., 2011. Deformation and secondary faulting associated with basement-involved compressional and extensional structures. AAPG Bull. 95 (4), 675–689. https://doi.org/10.1306/09131010007.

Morley, C.K., Nixon, C.W., 2016. Topological characteristics of simple and complex normal fault networks. J. Struct. Geol. 84, 68–84. https://doi.org/10.1016/j.jsg.2016.01.005.

Mukherjee, S., 2014. Review of flanking structures in meso- and micro-scales. Geol. Mag. 151 (6), 957–974. https://doi.org/10.1017/S0016756813001088.

Mukherjee, S., Tayade, L., 2019. Kinematic analysis of brittle roto-translational planar and listric faults based on various rotational to translational velocities of the faulted blocks. Mar. Petrol. Geol. 107, 326–333. https://doi.org/10.1016/j.marpetgeo.2019.04.024.

Oner, Z., Dilek, Y., 2013. Fault kinematics in supradetachment basin formation, Menderes core complex of western Turkey. Tectonophysics 608, 1394–1412. https://doi.org/10.1016/j.tecto.2013.06.003.

Padmalal, A., Khonde, N., Maurya, D.M., Shaikh, M., Kumar, A., Vanik, N., Chamyal, L.S., 2019. Geomorphic characteristics and morphologic dating of the Allah Bund Fault scarp, great rann of Kachchh, western India. In: Mukherjee, S. (Ed.), Tectonics and Structural Geology: Indian Context. Springer, Switzerland, pp. 55–74. https://doi.org/10.1007/978-3-319-99341-6_3.

Patidar, A.K., 2010. Neotectonic Studies in Southern Mainland Kachchh Using GPR with Special Reference to Katrol Hill Fault. Ph.D. thesis. The Maharaja Sayajirao University of Baroda, Vadodara, Gujarat. Retrieved from Shodhganga. http://hdl.handle.net/10603/59101.

Patidar, A.K., Maurya, D.M., Thakkar, M.G., Chamyal, L.S., 2007. Fluvial geomorphology and neotectonic activity based on field and GPR data, Katrol hill range, Kachchh, western India. Quat. Int. 159 (1), 74–92. https://doi.org/10.1016/j.quaint.2006.08.013.

Patidar, A.K., Maurya, D.M., Thakkar, M.G., Chamyal, L.S., 2008. Evidence of neotectonic reactivation of the Katrol Hill Fault during late quaternary and its GPR characterization. Curr. Sci. 338–346. Retrieved from. http://www.jstor.org/stable/24100341.

Patra, A., Saha, D., 2019. Stress regime changes in the Main Boundary Thrust zone, Eastern Himalaya, decoded from fault-slip analysis. J. Struct. Geol. 120, 29–47. https://doi.org/10.1016/j.jsg.2018.12.010.

Petit, J.-P., 1987. Criteria for the sense of movement on fault surfaces in brittle rocks. J. Struct. Geol. 9 (5-6), 597–608. https://doi.org/10.1016/0191-8141(87)90145-3.

Prucha, J.J., Graham, J.A., Nickelsen, R.P., 1965. Basement-controlled deformation in Wyoming province of rocky mountains foreland. AAPG (Am. Assoc. Pet. Geol.) Bull. 49 (7), 966–992. https://doi.org/10.1306/A663368A-16C0-11D7-8645000102C1865D.

Quintà, A., Tavani, S., Roca, E., 2012. Fracture pattern analysis as a tool for constraining the interaction between regional and diapir-related stress fields: poza de la Sal Diapir (Basque Pyrenees, Spain). Geological Society, London, Special Publications 363 (1), 521–532. https://doi.org/10.1144/SP363.25.

Rajendran, C.P., Rajendran, K., 2001. Characteristics of deformation and past seismicity associated with the 1819 Kutch earthquake, northwestern India. Bull. Seismol. Soc. Am. 91 (3), 407–426. https://doi.org/10.1785/0119990162.

Rastogi, B.K., Gupta, H.K., Mandal, P., Satyanarayana, H.V.S., Kousalya, M., Raghavan, R., Jain, R., Sarma, A.N.S., Kumar, N., Satyamurty, C., 2001. The deadliest stable continental region earthquake occurred near Bhuj on 26 January 2001. J. Seismol. 5 (4), 609–615. https://doi.org/10.1023/A:1012228507533.

Richardson, R.M., Solomon, S.C., Sleep, N.H., 1979. Tectonic stress in the plates. Rev. Geophys. 17 (5), 981–1019. https://doi.org/10.1029/RG017i005p00981.

Ricketts, J.W., Karlstrom, K.E., Kelley, S.A., 2015. Embryonic core complexes in narrow continental rifts: the importance of low-angle normal faults in the Rio Grande rift of central New Mexico. Geosphere 11 (2), 425–444. https://doi.org/10.1130/GES01109.1.

Ruppel, C., 1995. Extensional processes in continental lithosphere. J. Geophys. Res.: Solid Earth 100 (B12), 24187–24215. https://doi.org/10.1029/95JB02955.

Sasvári, Á., Baharev, A., 2014. SG2PS (structural geology to postscript converter)–A graphical solution for brittle structural data evaluation and paleostress calculation. Comput. Geosci. 66, 81–93. https://doi.org/10.1016/j.cageo.2013.12.010.

Schlische, R.W., 1995. Geometry and origin of fault-related folds in extensional settings. AAPG Bull. 79 (11), 1661–1678. https://doi.org/10.1306/7834DE4A-1721-11D7-8645000102C1865D.

Sen, S., Kundan, A., Kalpande, V., Kumar, M., 2019. The present-day state of tectonic stress in the offshore Kutch-Saurashtra Basin, India. Mar. Petrol. Geol. 102, 751–758. https://doi.org/10.1016/j.marpetgeo.2019.01.018.

Shaikh, M.A., Maurya, D.M., Vanik, N.P., Mukherjee, S., Chamyal, L.S., 2019a. Cenozoic kinematics of the seismically active western continental margin of the Indian plate. In: Poster presented at Tectonic Studies Group Annual General Meeting (TSG AGM), University of Bergen, Norway 100, 501.

Shaikh, M.A., Maurya, D.M., Vanik, N.P., Padmalal, A., Chamyal, L.S., 2019b. Uplift induced structurally controlled landscape development: example from fault bounded Jumara and Jara domes in Northern Hill Range, Kachchh, Western India. Geosci. J. 23 (4), 575–593. https://doi.org/10.1007/s12303-018-0061-9.

Shaw, B.E., 1995. Frictional weakening and slip complexity in earthquake faults. Journal of Geophysical Research: Solid Earth 100 (B9), 18239–18251. https://doi.org/10.1029/95JB01306.

Sibson, R.H., 1995. Selective fault reactivation during basin inversion: potential for fluid redistribution through fault-valve action. Geological Society, London, Special Publications 88 (1), 3–19. https://doi.org/10.1144/GSL.SP.1995.088.01.02.

Simón, J.L., 2019. Forty years of paleostress analysis: has it attained maturity? J. Struct. Geol. 125, 124–133. https://doi.org/10.1016/j.jsg.2018.02.011.

Simpson, I.R., Gravestock, M., Ham, D., Leach, H., Thompson, S.D., 1989. Notes and cross-sections illustrating inversion tectonics in the Wessex Basin. Geological Society, London, Special Publications 44 (1), 123–129. https://doi.org/10.1144/GSL.SP.1989.044.01.08.

Singh, B., Mandal, P., 2020. Upper mantle seismic anisotropy beneath the Kachchh rift zone, Gujarat, India, from shear wave splitting analysis. Journal of Earth System Science 129. https://doi.org/10.1007/s12040-020-1373-5.

Sippel, J., Scheck-Wenderoth, M., Reicherter, K., Mazur, S., 2009. Paleostress states at the south-western margin of the Central European Basin System—application of fault-slip analysis to unravel a polyphase deformation pattern. Tectonophysics 470 (1-2), 129–146. https://doi.org/10.1016/j.tecto.2008.04.010.

Sperner, B., Zweigel, P., 2010. A plea for more caution in fault–slip analysis. Tectonophysics 482 (1-4), 29–41. https://doi.org/10.1016/j.tecto.2009.07.019.

Stoneley, R., 1982. The structural development of the Wessex Basin. J. Geol. Soc. 139 (4), 543–554. https://doi.org/10.1144/gsjgs.139.4.0543.

Tiwari, S.K., Beniest, A., Biswal, T.K., 2020. Extension driven brittle exhumation of the lower-middle crustal rocks, a paleostress reconstruction of the Neoproterozoic Ambaji Granulite, NW India. J. Asian Earth Sci. 195, 104341. https://doi.org/10.1016/j.jseaes.2020.104341.

Tranos, M.D., 2017. The use of Stress Tensor Discriminator Faults in separating heterogeneous fault-slip data with best-fit stress inversion methods. J. Struct. Geol. 102, 168–178. https://doi.org/10.1016/j.jsg.2017.12.015.

Twiss, R.J., Unruh, J.R., 1998. Analysis of fault slip inversions: do they constrain stress or strain rate? J. Geophys. Res.: Solid Earth 103 (B6), 12205–12222. https://doi.org/10.1029/98JB00612.

Vanik, N., Shaikh, M.A., Mukherjee, S., Maurya, D.M., Chamyal, L.S., 2018. Post-Deccan Trap stress reorientation under transpression: evidence from fault slip analysis from SW Saurashtra, Western India. J. Geodyn. 121, 9–19. https://doi.org/10.1016/j.jog.2018.06.004.

Wallace, R.E., 1951. Geometry of shearing stress and relation to faulting. J. Geol. 59 (2), 118–130. Retrieved from. http://www.jstor.org/stable/30070473.

Williams, G.D., Powell, C.M., Cooper, M.A., 1989. Geometry and kinematics of inversion tectonics. Geological Society, London, Special Publications 44 (1), 3–15. https://doi.org/10.1144/GSL.SP.1989.044.01.02.

Withjack, M.O., Olsen, P.E., Schlische, R.W., 1995. Tectonic evolution of the Fundy rift basin, Canada: evidence of extension and shortening during passive margin development. Tectonics 14 (2), 390–405. https://doi.org/10.1029/94TC03087.

Xu, S.S., Nieto-Samaniego, Á.F., Alaniz-Álvarez, S.A., Velasquillo-Martínez, L.G., 2011. Effect of block rotation on the pitch of slickenlines. Cent. Eur. J. Geosci. 3 (1), 29–36. https://doi.org/10.2478/v10085-010-0031-6.

Yamaji, A., Sato, K., 2019. Stress inversion meets plasticity theory: a review of the theories of fault-slip analysis from the perspective of the deviatoric stress-strain space. J. Struct. Geol. 125, 296–310. https://doi.org/10.1016/j.jsg.2019.03.003.

Yin, Z.M., Ranalli, G., 1992. Critical stress difference, fault orientation and slip direction in anisotropic rocks under non-Andersonian stress systems. J. Struct. Geol. 14 (2), 237–244. https://doi.org/10.1016/0191-8141(92)90060-A.

Zalohar, J., Vrabec, M., 2007. Paleostress analysis of heterogeneous fault-slip data: the Gauss method. J. Struct. Geol. 29 (11), 1798–1810. https://doi.org/10.1016/j.jsg.2007.06.009.

Zoback, M.L., Zoback, M.D., Adams, J., et al., 1989. Global patterns of tectonic stress. Nature 341 (6240), 291. https://doi.org/10.1038/341291a0.

Zoback, M.L., 1992. First-and second-order patterns of stress in the lithosphere: the World Stress Map Project. J. Geophys. Res.: Solid Earth 97 (B8), 11703–11728. https://doi.org/10.1029/92JB00132.

Zwaan, F., Schreurs, G., 2020. Rift segment interaction in orthogonal and rotational extension experiments: implications for the large-scale development of rift systems. J. Struct. Geol. https://doi.org/10.1016/j.jsg.2020.104119.